INTEGRATION OF TIME-LAPSE SEISMIC DATA USING THE ONSET TIME APPROACH: THE IMPACT OF SEISMIC SURVEY FREQUENCY

A Thesis

by

TIAN LIU

Submitted to the Office of Graduate and Professional Studies of
Texas A&M University
in partial fulfillment of the requirements for the degree of

MASTER OF SCIENCE

Chair of Committee,	Akhil Datta-Gupta
Co-Chair of Committee,	Michael J. King
Committee Member,	Debjyoti Banerjee
Head of Department,	Jeff Spath

May 2019

Major Subject: Petroleum Engineering

ABSTRACT

The seismic inversion method using the seismic onset times has shown great promise for integrating frequent seismic surveys for updating geologic models. However, due to the high cost of seismic surveys, frequent seismic surveys are not commonly available. In this study, we focus on analyzing the impact of seismic survey frequency on the onset time approach, aiming to extend the advantages of onset time approach when infrequent seismic surveys are available.

To analyze the impact of seismic survey frequency on the onset time approach, first, we conduct a sensitivity analysis based on the frequent seismic survey data (over 175 surveys) of steam injection in a heavy oil reservoir (Peace River Unit) in Canada. The calculated onset time maps based on seismic survey data sampled at various intervals from the frequent data sets are compared to examine the need and effectiveness of interpolation between surveys. Additionally, we compared the onset time inversion with traditional seismic amplitude inversion and quantitatively investigate the nonlinearity and robustness for these two inversion methods.

The sensitivity analysis shows that using interpolation between seismic surveys to calculate the onset time, an adequate onset time map can be extracted from the infrequent seismic surveys. This holds good as long as there are no changes in the underlying physical mechanisms during the interpolation period. It is concluded that the linear interpolation is more efficient and robust than the Lagrange interpolation. A 2D waterflooding case demonstrates the necessity of interpolation for resolving into the large time span between

the seismic surveys and obtaining more accurate model update and more efficient misfit reduction. The Brugge benchmark case shows that the onset time inversion method obtains comparable permeability update as the traditional seismic amplitude inversion method while being much more efficient. This results from the significant data reduction achieved by integrating a single onset time map rather than multiple sets of amplitude maps. The onset time approach also achieves superior convergence performance, resulting from its quasi-linear properties. It is found that the nonlinearity of the onset time method is smaller than that of the amplitude inversion method by several orders of magnitude.

DEDICATION

To my beloved parents Xiangen Liu and Dongxiang Wang, and my family members, for their unconditional love and support.

ACKNOWLEDGEMENTS

I would like to thank my committee chair, Dr. Akhil Datta-gupta, for providing academic guidance and financial support throughout my study at TAMU. Also, I appreciate his understanding and support for helping me against difficulties.

Also, I would like to thank my co-chair, Dr. Michael J. King and my committee member Dr. Debjyoti Banerjee, for their guidance and support throughout the course of this research.

Thanks also go to my MCERI colleagues, especially Gill Hetz, Hongquan Chen, Xu Xue, Rongqiang Chen, Atsushi Iino, Hyunmin Kim etc. I would like to thank them for their patient teaching and guidance throughout my research work. Moreover, I would like to thank Ms. Phaedra Hopcus for her generous help with all my life and study.

Additionally, I would like to thank my friends at TAMU for their friendship and help during my stay in the United States.

Finally, thanks to my mother and father and my family members for their encouragement, patience and love.

CONTRIBUTORS AND FUNDING SOURCES

Contributors

This work was supervised by a thesis committee consisting of Professor Akhil Datta-Gupta (advisor), Michael J. King (co-advisor) of the Department of Petroleum Engineering and Professor Debjyoti Banerjee of the Department of Mechanical Engineering.

The idea of applying interpolation for calculating the seismic onset time map with infrequent seismic data was proposed through the discussion between the student and Dr. Akhil Datta-gupta and Dr. Gill Hetz. The comparison of nonlinearity part was further investigated and validated based on the previous work of Dr. Gill Hetz. The proposed onset time inversion workflow was implemented by the student with the in-house software Destiny, which was originally developed by Hongquan Chen. The Peace River model and time shift seismic data were provided by Dr. Gill Hetz based on his previous work with Shell.

All the other coding, testing, applications and validation work for this study were completed by the student independently.

Funding Sources

This work was made possible by the financial support of the member companies of the Model Calibration and Efficient Reservoir Imaging (MCERI) consortium, and a U.S. Department of Energy Grant, DE-FE0031625.

TABLE OF CONTENTS

Page

LIST OF FIGURES

Page

LIST OF TABLES

Page

CHAPTER I

INTRODUCTION

The integration of seismic data into the high-resolution geologic model, also known as seismic inversion, provides great potential for calibrating reservoir parameters, which enables better understanding of the reservoir sweep and flow patterns. This is because the seismic data are usually spatially dense with a good spatial resolution, while the production data are usually finely sampled in time but spatially averaged. The valuable spatial information provided by the seismic data can be used to recover the large scale geologic feature of the reservoir that is far away from the well through a history matching approach. As a result, the reservoir connectivity can be updated by recovering the low permeability flow barriers (shale layers and sealing faults) and the highly permeable flow channels etc.

In this chapter, first, the development of the onset time inversion method is introduced. Then, the objectives of this research and the outline of the thesis are summarized.

1.1 Background and Literature Review

With the fast development of seismic monitoring technology, the use of time-lapse (4D) seismic data for the characterization of the subsurface flow has become increasing popular. A number of successful field applications of reservoir management based on 4D seismic data have demonstrated its power and efficacy (Behrens et al., 2002; Fahimuddin

et al., 2010; Landrø et al., 2001; Landrø et al., 1999; Watanabe et al., 2017; Hetz et al., 2017). The integration of 4D seismic data into high-resolution geologic model usually involves least-squares-based minimization to match the simulated seismic response and the observed seismic signals (Dadashpour, Mohsen et al., 2010; Dadashpour et al., 2009; Falcone et al., 2004; Gosselin et al., 2003; Gosselin et al., 2001; Rey et al., 2009; Rey et al., 2012; Rwechungura, R.W. et al., 2012; Vasco, 2004; Watanabe et al., 2017; Tang et al., 2018). The objective function has mostly focused on matching the seismic amplitude, travel-time, waveform, etc. This inverse problem is usually highly nonlinear and ill-posed, which results in the non-unique solution and can easily cause the solution to converge to a local minimum, leading to an inadequate history match (Cheng et al., 2005).

For the recent years, the seismic inversion method based on the seismic onset times has shown great potential for integrating 4D seismic data into high-resolution geologic models (Hetz et al., 2017; Vasco et al., 2015; Vasco et al., 2014). Vasco et al. (2014) introduced the seismic onset time as the calendar time at which a measured quantity, such as seismic travel time or a reflection amplitude, begins to deviate from its background value. Using the concept of seismic onset time, multiple sets of 4D seismic data can be converted into a single onset time map, which can be used for dynamic model updating (Hetz et al., 2017).

Vasco et al. (2014) demonstrated the utilities of seismic onset times based on a field case with continuous seismic surveys, which were conducted to monitor the movement of carbon dioxide injected into a permeable sand formation at the Frio pilot site near Houston, Texas. Using an iterative inversion algorithm, the permeability variations

between boreholes were estimated. It was shown that the onset times are not very sensitive to the choices of petro-elastic model, but strongly influenced by the saturation changes within the formation, especially the break-through time of the injected fluids.

Vasco et al. (2015) further investigated the robustness of the onset time for handling noisy seismic data. It was shown that reliable onset time map could still be extracted from the noisy data. Moreover, test on the seismic survey intervals indicated that large-scale permeability variations could be recovered even if the seismic surveys were placed as much as 300 days apart.

Hetz et al. (2017) has proposed a novel and efficient seismic inversion workflow to integrate frequent seismic surveys into the reservoir model, which involves both global and local stage matching of the seismic onset time map. He has successfully implemented this method for a heavy oil reservoir in Canada where daily time-lapse seismic surveys are recorded by the permanently buried seismic monitoring system, which was deployed to monitor the steam injection process (Hetz et al., 2017). The onset time inversion method was shown to be extremely efficient by compressing hundreds of time shift maps into just a single onset time map. The updated model obtains improved estimation of the permeability distribution, fluid saturation evolution and swept volume.

1.2 Objectives and Thesis Outline

The onset time inversion method has shown its efficacy and robustness for integrating frequent seismic surveys, where the propagation of saturation front could be captured in details with the short time span between seismic surveys. However, due to the

high cost associated with conducting seismic surveys, frequent seismic surveys are usually not commonly available. For most field situations, seismic surveys are usually conducted every several years, which is infrequent in time. Without the high time resolution in the time-lapse seismic data, question arises that whether the onset time inversion method could still be applied for integrating the infrequent seismic data. This question defines the objectives of this study.

In this study, I focus on investigating the feasibility of onset time inversion method for integrating infrequent seismic surveys and comparing the inversion performance of onset time inversion method with the traditional amplitude inversion method. The main objectives and corresponding chapters of this thesis are listed as followed.

(1) In Chapter II, the onset time inversion workflow is illustrated with a 2D synthetic case. The calculation of onset time map, petro-elastic model used for interpreting the seismic data, and the calculation of onset time sensitivity, as well as the formulation of objective function are elaborated in details.

(2) In Chapter III, I present the results of sensitivity analysis on the impact of seismic survey frequency. The onset time maps calculated based on the infrequent seismic data sampled from the frequent seismic data of Peace River project are compared. Also, different interpolation methods are compared for resolving into the large time span between seismic surveys for an accurate onset time map. The limitations of onset time approach are analyzed with the Peace River case. Moreover, the sensitivity of the onset time map to the selection of threshold value is analyzed based on a 2D waterflooding case.

(3) In Chapter IV, I compared the inversion performance of the onset time inversion method with the traditional amplitude inversion method using both 2D synthetic and SPE Brugge Benchmark case. Additionally, the nonlinearity associated with these two methods are quantitatively investigated by applying the geometric concept of nonlinearity.

(4) Finally, in Chapter V, the conclusions of my research work and the value of the onset time approach are discussed. In addition, recommendations for future work are summarized.

CHAPTER II

METHODOLOGY AND FORMULATION*

In this chapter, the onset time inversion workflow is introduced in details. A 2D synthetic case is used to illustrate the methodology for converting multiple sets of time-lapse seismic data into a single onset time map. In addition, the choice of threshold value, petro-elastic model, formulation of sensitivity, and objective function are discussed in details.

2.1 Onset Time as Seismic Observation

The onset times (Vasco et al., 2015) are defined as the calendar times at which the measured time-lapse attributes begin to deviate from their initial or background values above a pre-defined threshold value. Using the onset time approach, multiple sets of time-lapse seismic data can be converted into a single onset time map, which represents the propagation of the change (change in the fluids saturation, pressure, temperature, etc.) within the reservoir.

To illustrate the onset time approach, a 2D synthetic case with five-spot waterflooding pattern is shown below (Figure 2.1). Suppose 5 sets of time-lapse seismic surveys were conducted over a waterflooding process of 2200 days. Every two

* Part of this section is reprinted with permission from "Seismic Onset Time Inversion Method for Infrequent Seismic Surveys" by T. Liu, 2018. Paper 1940440 prepared for presentation at the SPE Annual Technical Conference and Exhibition held in Dallas, Texas, USA, 24 September –26 September.

consecutive seismic surveys are either 400 or 600 days apart, which are sparse in time. The observed acoustic impedance maps and the methodology to calculate the onset time map for infrequent seismic surveys are shown in Figure 2.2. It can be observed from the plot that for the same location, the acoustic impedance values increase with time because of the increase in the saturated rock density and p-wave velocity, resulting from the lighter fluid replaced by the heavier fluid, which is the oil replaced by the injected water.

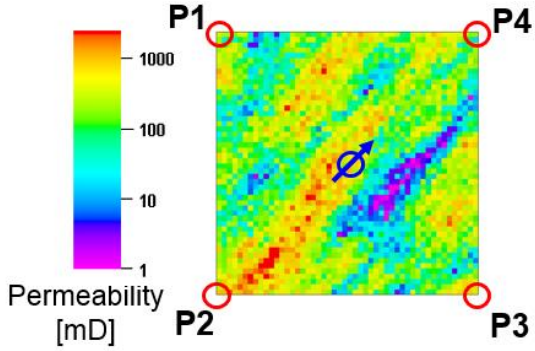

Figure 2.1 2D (50x50) waterflooding case

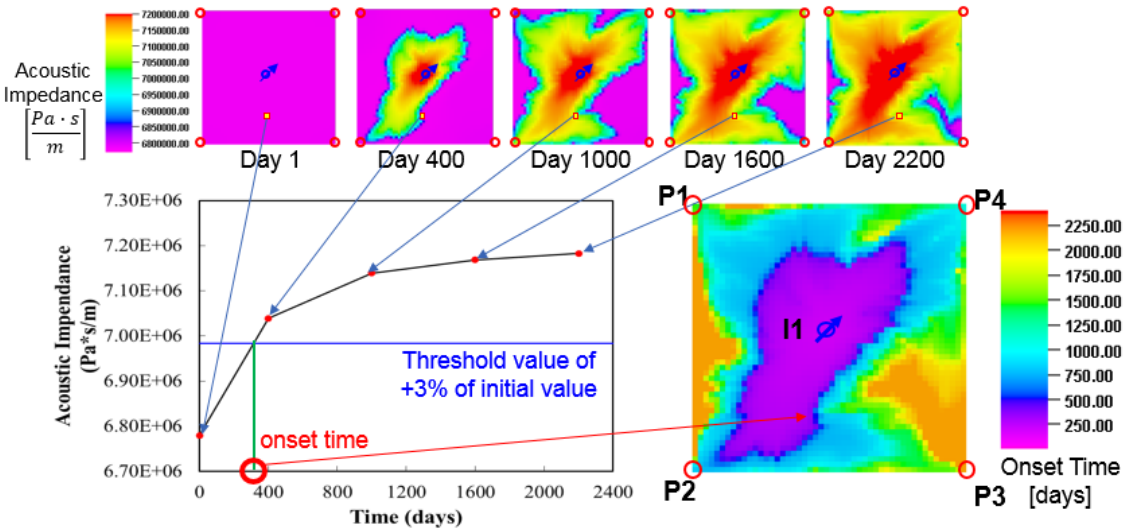

Figure 2.2 Onset time calculation for infrequent seismic surveys (reprinted with permission from Liu et al., 2018)

The first step of to calculate the onset time map is to define a threshold value that characterizes the onset of the dominant change in the reservoir, such as the arrival of the injected water or the propagation of pressure front etc. In this 2D example, the threshold value is chosen to be an increase in the acoustic impedance of 3% of the initial values, based on the seismic response of the unswept region. A detailed explanation for the choice of threshold value is discussed later in section 3.5. After defining a threshold value, for a certain location, the earliest observed seismic data point that exceeds the threshold value is identified as the onset point. Then, linear interpolation is conducted to calculate the interpolated time at the threshold value. The interpolated time is chosen as the onset time for this location. It should be noted that because of the large time span between seismic surveys, interpolation is required to find an accurate and meaningful onset time for infrequent seismic data. However, for frequent seismic data, the interpolation is not mandatory because of the short time span between seismic surveys. In that case, the seismic survey time of the point that has crossed the threshold value is chosen as the onset time (Hetz et al., 2017). A detailed comparison between using interpolation and not using interpolation is shown in section 3.3.

Following the procedure described above to find the onset time for all the location, an onset time map could be obtained, which clearly represents the travel time of the water saturation front to propagate from the injector to each spatial location. One of the advantages of the onset time approach is the significant data reduction achieved by reducing multiple sets of seismic amplitude maps into a single onset time map.

Another advantage of the onset time approach lies in its robustness with regarding to different petro-elastic models, which were used to interpret the seismic data. The following Figure 2.3 shows the acoustic impedance change (seismic amplitude) maps and the onset time maps calculated based on Reuss lower bound and Vogit upper bound (Mavko et al., 2009). The Reuss and Vogit bounds are two different model used to describe the bulk modulus of the pore-filling fluids, which will affect the seismic velocity.

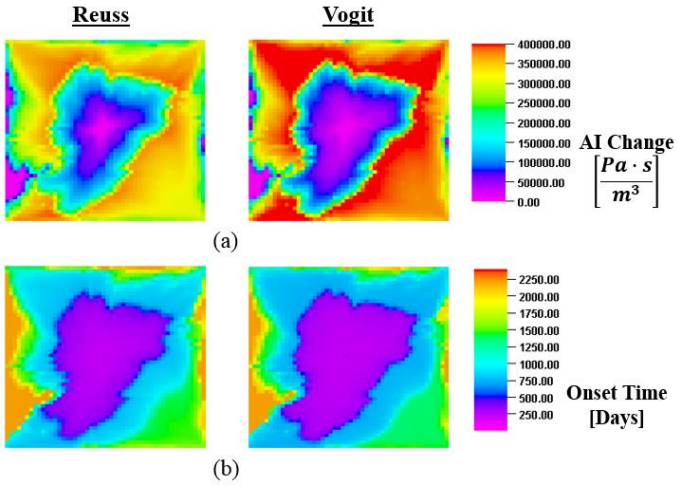

Figure 2.3 Effects of petro-elastic models (a) acoustic impedance change maps between the first and last survey time and (b) onset time maps (reprinted with permission from Liu et al., 2018)

Obviously, as can be seen in Figure 2.3, the calculated amplitude change maps show many differences between each other, while the onset time maps are pretty similar. This is because the onset time represents the travel time of the fluid saturation front or pressure front. The onset time is more sensitive to the reservoir flow properties, such as the permeability and porosity. And it is less sensitive to the petro-elastic model (Vasco et al., 2014), making it a more robust seismic inversion method against the uncertainty in the seismic inversion results.

2.2 Seismic Onset Time Inversion Workflow

The onset time map is a valuable representation of the propagation of change in the reservoir, which can be used for dynamic modeling and model calibration through a history matching process. The onset time inversion workflow for integrating time-lapse seismic data is shown in the following Figure 4. The objective of seismic inversion is to update the prior model parameter based on the observed seismic data. The seismic inversion is conducted in an iterative manner by updating the reservoir model parameters iteratively until a desired match between the simulated onset time map and the observed seismic onset time map is achieved.

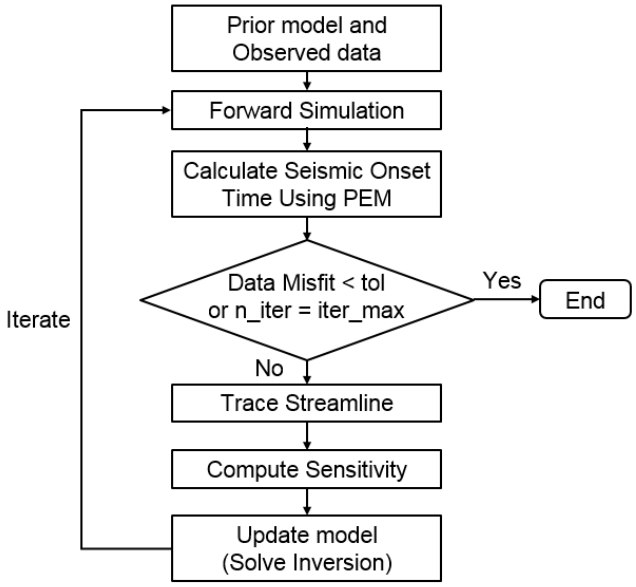

Figure 2.4 Onset time inversion workflow

The onset time inversion workflow starts with a prior geologic model and observed seismic onset time data. First, forward simulation is run based on the prior model to generate the prior reservoir response, including the fluids saturation, pore pressure and

temperature, etc. Then based on the reservoir response, the petro-elastic model (PEM) is used to calculate the simulated seismic onset time of the model. After obtaining the simulated seismic onset time, the next step is to calculate the data misfit. For the onset time inversion method, multiple sets of seismic data are converted into a single onset time map (Hetz, et al., 2017). Thus, the data misfit is the difference between the simulated onset time map and the observed onset time map.

Then, the streamlines are traced based on the cell face flux information obtained from the forward simulation. The streamline-based sensitivities are calculated with the time-of-flight information of the streamlines (Datta-Gupta and King, 2017). With the data misfit and sensitivity obtained, the next step is to obtain the update in model parameter by solving the minimization problem of the objective function. Afterwards, a forward simulation is run again based on the updated model, and the new data misfit is calculated in the same manner. The workflow is iterated until the stopping criteria has been satisfied, which is either the data misfit is less than a tolerance number, i.e. obtaining a desired match, or the number of iterations has reached the maximum number of iterations allowed.

2.3 Petro-elastic Model

In order to relate the change in the reservoir properties to the geophysical observations, a petro-elastic model is needed to calculate the rock elastic properties, such as the P-wave velocity, S-wave velocity, acoustic impedance, travel time, etc. The rock elastic properties vary in time because of the change in the dynamic reservoir properties, such as pore pressure, fluids saturation, temperature, etc.

The Gassmann's equation (1951) is used to estimate the changes in the rock elastic properties as a result of the fluid substitution and the change in the pore pressure and temperature, etc.

$$K_{\text{sat}} = K_{\text{fr}} + \frac{\left(K_{\text{HM}} - K_{\text{fr}}\right)^2}{K_{\text{HM}}\left(1 - \phi + \phi\frac{K_{\text{HM}}}{K_{\text{f}}} - \frac{K_{\text{fr}}}{K_{\text{HM}}}\right)} \tag{2.1}$$

K_{fr} is the bulk modulus of the porous rock frame, ϕ is the effective porosity of the medium. The bulk modulus of the mineral matrix K_{HM} is calculated based on Hertz-Mindlin contact theory (Mindlin 1949), and K_{f} is the bulk modulus of the pore-filling fluids.

The Gassmann's relation is valid in most practical cases, while it can have considerable uncertainty, particularly in the model used to calculate the K_{f}. The K_{f} is affected by: (1) the volume fraction of the phases; (2) the elastic moduli of each phase; (3) how the fluids are arranged within the pore space. From the simulation result and PEM, one can only specify the volume fractions and the constituent moduli. As of today, there is no universally accepted method of saturation mapping for the distribution of fluids within the reservoir (Vasco et al., 2015). Thus, one can only predict the lower bound and upper bound of K_{f}.

The Reuss lower bound is given by the following Eq.2.2.

$$K_f^{Reuss} = \left(\sum_{i=1}^{N}\frac{S_i}{K_i}\right)^{-1} \tag{2.2}$$

S_i is the saturation of the i$^{\text{th}}$ fluid and K_i is the bulk modulus of the i$^{\text{th}}$ fluid. The lower bound is obtained when the compression (propagation) is in a direction that is

perpendicular to the layers of pure components. Then the weakest layer determines the modulus (Vasco et al., 2015).

The Voigt upper bound is given by the Eq.2.3. The upper bound represents a scenario when the components are arranged in parallel to the direction of compression. Thus, the stiffest layer controls the modulus.

$$K_f^{Voigt} = \left(\sum_{i=1}^{N} S_i * K_i \right) \tag{2.3}$$

With the upper bound and lower bound defined, any estimate of the bulk modulus of the pore-filling fluids will fall between the bounds. The Hill estimate of the fluid bulk modulus (Mavko et al., 2009) gives the arithmetic average of the Voigt and Reuss bounds, as shown in the following Eq.2.4.

$$K_f^{Hill} = \frac{K_f^{Voigt} + K_f^{Reuss}}{2} \tag{2.4}$$

The density of the saturated rock is given by the weighted average of the rock matrix density and the components' density within the pores.

$$\rho_{sat} = (1-\phi)\rho_{ma} + \phi(S_o\rho_o + S_w\rho_w + S_g\rho_g) \tag{2.5}$$

Then, the P-wave velocity for an isotropic, layered, elastic medium (Kennett 1983) is defined as

$$V_p = \sqrt{\frac{K_{sat} + \frac{4}{3}G_{fr}}{\rho_{sat}}}. \tag{2.6}$$

In Eq.2.6, G_{fr} is the frame shear modulus, ρ_{sat} is the density of the saturated rock, and K_{sat} is the bulk modulus of the saturated rock, which is calculated by Eq.2.1.

Finally, the acoustic (P-wave) impedance is given by

$$Z_p = \rho_{sat} V_p = \sqrt{\rho_{sat}(K_{sat} + \frac{4}{3} G_{fr})}\,. \tag{2.7}$$

The following Figure 2.5 shows the P-wave velocities calculated using three petro-elastic models. Clearly, large differences exist between the calculated P-wave velocities, indicating the seismic interpretation is strongly dependent on the choice of petro-elastic model. As a result, considerable uncertainty can be introduced in the seismic inversion process. However, as shown in section 2.1, the onset time map is less sensitive to the choice of petro-elastic model and is a more robust method against the uncertainty in the inversion results.

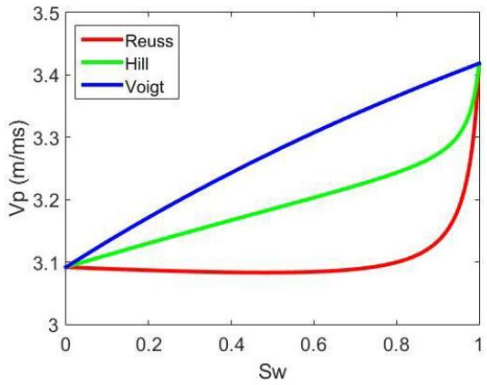

Figure 2.5 The compressional wave velocity as a function of water saturation for different petro-elastic models (reprinted from Hetz et al., 2017)

2.4 Onset Time Sensitivity

The sensitivity reflects the relation of the change in the seismic response with respect to the change in the model parameter. In this study, the semi-analytic streamline-based sensitivity is used to relate the onset time with the reservoir permeability, which can be efficiently computed with a single forward simulation (Datta-Gupta and King, 2017). Assuming the onset time is a function of fluids saturation and pressure, using the chain

rule, the onset time sensitivity with respect to the permeability at a given location can be derived as

$$G_{OT} = \frac{\delta OT}{\delta k} = \left[\frac{\partial OT}{\partial S_w} \frac{\partial S_w}{\partial k} + \frac{\partial OT}{\partial S_g} \frac{\partial S_g}{\partial k} + \frac{\partial OT}{\partial p} \frac{\partial p}{\partial k} \right]. \quad (2.8)$$

It should be noted that the seismic response is affected by multiple factors at the same time, including the change in the fluids saturation, the change in the pressure and temperature, etc. For example, during the waterflooding process, the increase in the water saturation will result in the increase in the acoustic impedance. While the reservoir pressure will also increase because of the injection of water, which will lead to the decrease in the acoustic impedance. Here, only the contribution of the dominant physics will be considered. Therefore, in the waterflooding case, since the dominant physics is the injected water displacing the oil, the contribution of the change in the gas saturation and pressure will be neglected.

In the above Eq. 2.8, $\frac{\partial OT}{\partial S_w}$ is computed numerically with the petro-elastic model by adding a perturbation to the water saturation using Eq.2.5 through Eq.2.7. The water saturation front sensitivity $\frac{\partial S_w}{\partial k}$ is computed semi-analytically (Datta-Gupta and King, 2017) based on the time-of-flight information along the streamlines using the following Eq.2.9.

$$\frac{\partial S_w}{\partial k} = -\frac{t}{\tau} \frac{S_w(\tau, t) - S_w(\tau, t - \Delta t)}{\Delta t} \frac{\delta \tau}{\delta k} \quad (2.9)$$

The Δt is the timestep size, and the above Eq.2.9 gives the saturation sensitivity at location τ at a given time t. The partial derivative of travel time with respect to permeability can be obtained from the following Eq.2.10 (Datta-Gupta and King, 2017).

$$\frac{\delta\tau(\psi)}{\delta k(x)} = \int_{inlet}^{outlet} \left[\frac{-s(x)}{k(x)} \right] dr = -\frac{\Delta\tau(x)}{k(x)} \tag{2.10}$$

The $\Delta\tau$ is the duration time for the tracer to travel (time-of-flight) across the current grid cell block. The k is the permeability of the current block. A detailed derivation of the time-of-flight and saturation front sensitivity is given in the Appendix A, B and C.

2.5 Objective Function

With sensitivity computed, the data integration leads to the minimization problem of the objective function. In this study, the penalized misfit function (He et al., 2002; Vasco and Datta-Gupta, 2016; Vasco et al., 1999) is adopted.

$$F(\delta k) = \|\delta d - G\delta k\| + \beta_1 \|\delta k\| + \beta_2 \|L\delta k\| \tag{2.11}$$

In the function above, F is the objective function. δd is the data misfit. The matrix G contains the sensitivities of the model responses with respect to the reservoir parameters. δk is the vector of the updates of reservoir model parameter and L is the second spatial difference operator matrix. The first term on the right-hand side of Eq.2.11 ensures the difference between the observed data and the calculated model predictions is minimized. The second term is the norm penalty, which penalizes the deviation of the updated model from the prior model. The third term is the roughness penalty, constraining the update in the model to be spatially smooth and consistent with the low-resolution of data. The

weights β_1 and β_2 determine the relative strength of the constraints on the prior model and roughness conditions. The choice of the weights reflects the confidence on the prior model and resolution of the data. In field applications, usually large weights are used in the beginning of the iterations to anchor the updated model to the prior model. Then, the constraints are gradually released with iterations to achieve desirable data misfit reduction. The minimization problem is solved with the LSQR algorithm (Paige and Saunders, 1982), which is well-suited for the highly ill-conditioned system.

CHAPTER III

SENSITIVITY ANALYSIS ON THE IMPACT OF SEISMIC SURVEY FREQUENCY AND SELECTION OF THRESHOLD VALUE

Onset time approach has shown great potential for frequent seismic data integration (Hetz et al., 2017). However, frequent seismic surveys are usually not commonly available because of the high cost associated with conducting seismic surveys. To investigate the applicability of onset time approach for infrequent seismic data integration, this chapter presents the results of the sensitivity analysis on the impact of the seismic survey frequency.

In this chapter, first the Peace River project is introduced to demonstrate the onset time approach for frequent seismic data integration. The physical change related to the change in the time shift data in the Peace River project is discussed. Then, sensitivity analysis is conducted to analyze the impact of seismic survey frequency on the onset time pattern. Additionally, a 2D synthetic case is used to show the necessity of interpolation for calculating onset time from infrequent seismic data. The limitations of the onset time approach for seismic inversion are also discussed. Moreover, we discussed the criteria for selecting the threshold value and conducted sensitivity analysis on the selection of threshold values with a 2D waterflooding case.

3.1 Onset Time Approach for the Peace River Project

In this section, we introduce the frequent seismic data in the Peace River project and discuss the approach to calculate the onset time map. In addition, we discuss the possible physical causes of the change in the seismic response.

3.1.1 Introduction of the Peace River Reservoir

The Peace River reservoir is a heavy oil reservoir located in southwestern Alberta (Figure 3.1), Canada, which was discovered in 1951. It is the smallest of the four large deposits of oil sands of the Western Canadian Sedimentary Basin formation. It contains large amount of bitumen deposit of 7~10 API degrees with in-place reserve of 155 billion barrels (Zhou, et al., 2007; Lopez, et al., 2015). The oil mainly located in the lower Cretaceous Bluesky formation with siliciclastic sediments deposited in a marginal marine setting. The payzone is a highly unconsolidated sand formation with an average thickness of 25 m. It is located around 550 m below the surface, sealing by the top marine Wilrich shale and separated from the bottom Paleozoic carbonate by an unconformity. The reservoir temperature is around 16~22 ℃, under which the oil has a large viscosity of $0.1\sim8\times10^5$ cP. Considering the small thickness of the formation and high viscosity of oil, steam injection with multilateral wells were deployed to stimulate the production. The Pad 31 is the focus of this study.

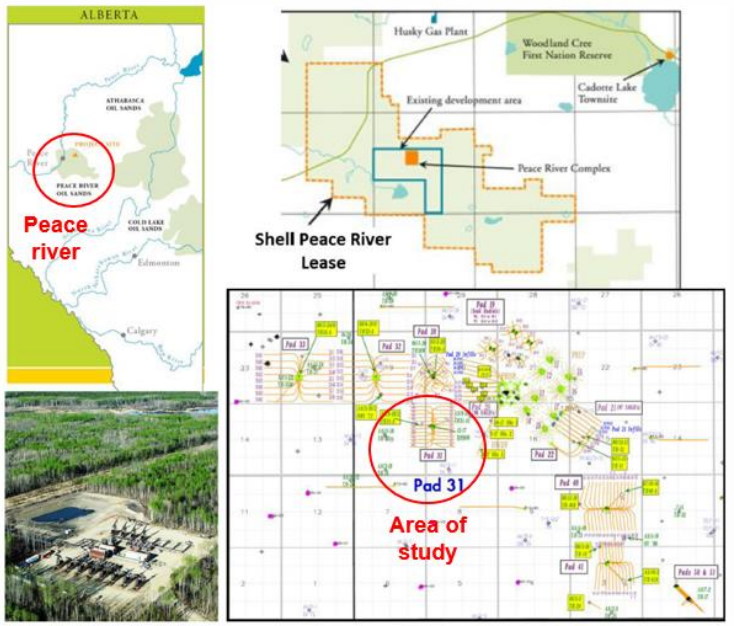

Figure 3.1 Location of the Peace River reservoir and the Pad 31 (area of study) (reprinted from Lopez, et al. 2015)

3.1.2 Introduction of Frequent Seismic Surveys

The Peace River unit (Pad 31) began operation in 2001 and has been undergoing several thermal recovery schemes including the Cyclic Steam Stimulation (CSS) and Steam Assisted Gravity Drainage (SAGD) to increase the recovery of the heavy bitumen deposit. Because of insufficient stimulation of the reservoir volume, the recovery of heavy resources is pretty limited. To better understand the sweeping and propagation of the steam front, the world's largest SeisMovie permanent seismic monitoring system was deployed in 2014 in Pad 31 to monitor the injection and production. The permanently buried sources and sensors were used to monitor the reservoir on a daily basis (Hetz et al., 2017; Lopez et al., 2015). Figure 3.2 shows the placement of the steam injectors and producers, where six new horizontal steam injectors (shown in green) were drilled and operated as Top

Down Steam Drive (TDSD). In addition to the ongoing TDSD, one of the producers (31-08 well) has undergone CSS to promote the communication with the northern part of the pad.

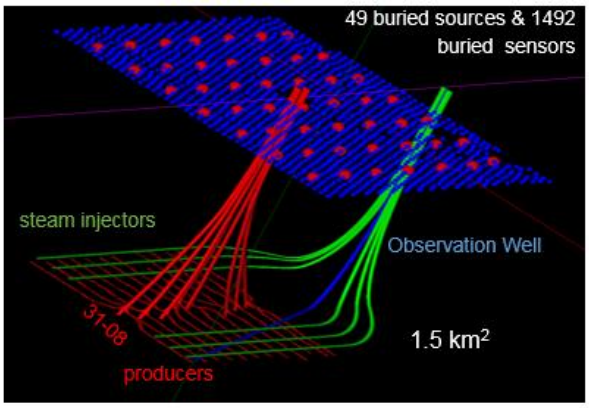

Figure 3.2 Pad 31 horizontal production wells (red), injection wells (green), and observation well (blue). Also shown are seismic sources (red dots) and receivers (blue dots). Producer 31-08 underwent CSS and is the focus of this study (reprinted from Hetz et al., 2017)

The recorded seismic data is translated into time shift maps, expressing the travel time changes in the seismic wave propagation across the entire reservoir between a chosen baseline survey (i.e. the start of the steam injection cycle) and subsequent monitor surveys. An illustration of the two-way travel time is shown in the following Figure 3.3.

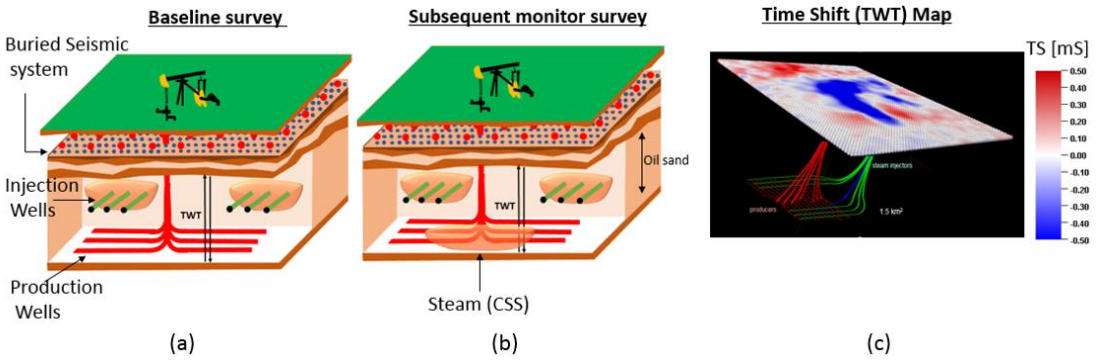

Figure 3.3 Illustration of the two-way travel time and time shift calculation. (a) Travel time of acoustic waves across the reservoir for the baseline survey at the beginning of steam injection. (b) Travel time of subsequent monitor surveys. (c) Time shift maps based on the difference of two-way travel times (reprinted from Hetz et al., 2017)

The time shift value, i.e. the two-way travel time change is calculated as shown in the following Eq. 3.1.

$$ts_{\text{survey i}} = t_{\text{survey i}} - t_{\text{baseline survey}} = \left(\frac{L}{V_{pi}} - \frac{L}{V_{pb}}\right) \tag{3.1}$$

The $t_{\text{survey i}}$ and $t_{\text{baseline survey}}$ are the two-way travel time of P-wave across the entire reservoir formation for the subsequent survey i and the chosen baseline survey. The V_{pi} and V_{pb} are the velocity of P-wave for the subsequent survey i and the chosen baseline survey, which can be calculated by Eq. 2.6. L is the vertical distance between the sensors and a particular point in the reservoir.

Over one CSS cycle for well 31-08, total 175 time-lapse time shift maps (Figure 3.4) are available for integration. The red color in the Figure 3.4 represents the velocity "slow down" while the blue color indicates the velocity "speed up". Previous studies (Lopez et al., 2015, Przybysz-Jarnut et al., 2015, La Follett et al., 2015) interpreted the velocity "slow down" as a result of the increases in the reservoir pressure (pulling sand

grains apart) or the increases in the temperature (softening the cold bitumen) or replacement of "harder" for "softer" reservoir fluids (e.g. water or oil being displaced by gas coming out of solution). On the contrary, the velocity "speed up" results from the opposite effects, such as the water replacing the gas that goes back to solution or is produced reducing the gas saturation, or the decreases in the pressure and temperature because of production.

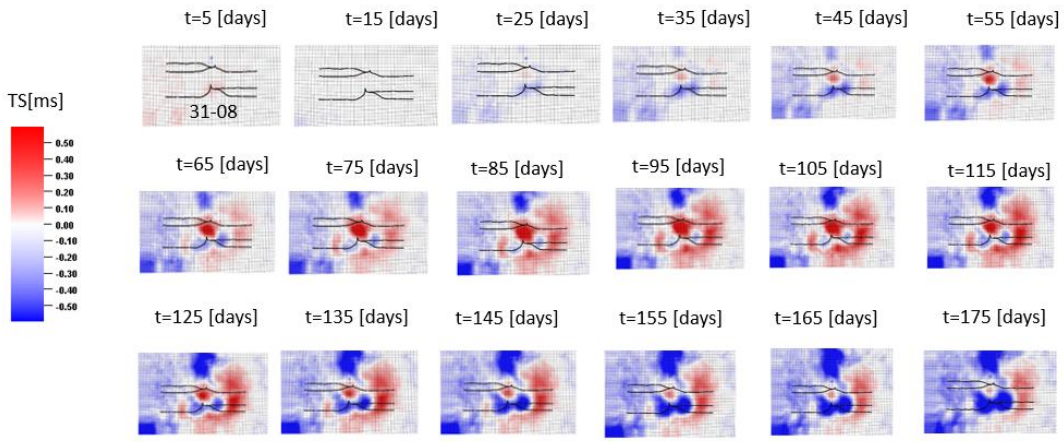

Figure 3.4 Seismic observations in well 31-06 (lower one) and well 31-06 (upper one). 18 samples of time shift maps are shown out of 175 time shift maps that are available for integration (reprinted from Hetz et al., 2017)

3.1.3 Multiple Time Shift Maps to a Single Onset Time Map

The challenges for integrating these seismic data include large amounts of data and no clear patterns between the time shift maps, which makes it extremely difficult for seismic data integration. To solve the problem, Hetz et al. (2017) proposed a novel onset time approach, which compresses multiple sets of seismic data into a single onset time map, obtaining significant data reduction. In the Peace River case, during the steam injection process, the injected steam / condensed water displaced the gas in the formation,

resulting in the increasing formation density and faster traveling speed of the P-wave. Thus, the two-way travel time decreases, leading to the negative time shift values. Based on the signal-to-noise ratio, the onset time is chosen as the time at which the observed time shift value decreases below -0.09 ms. The calculated onset time map as shown in Figure 3.5(c) clearly shows the propagation of the steam front around the wellbore during the steam injection period (first 85 days). More details for calculating the onset time map for the Peace River case can be found in Hetz et al.'s paper (2017).

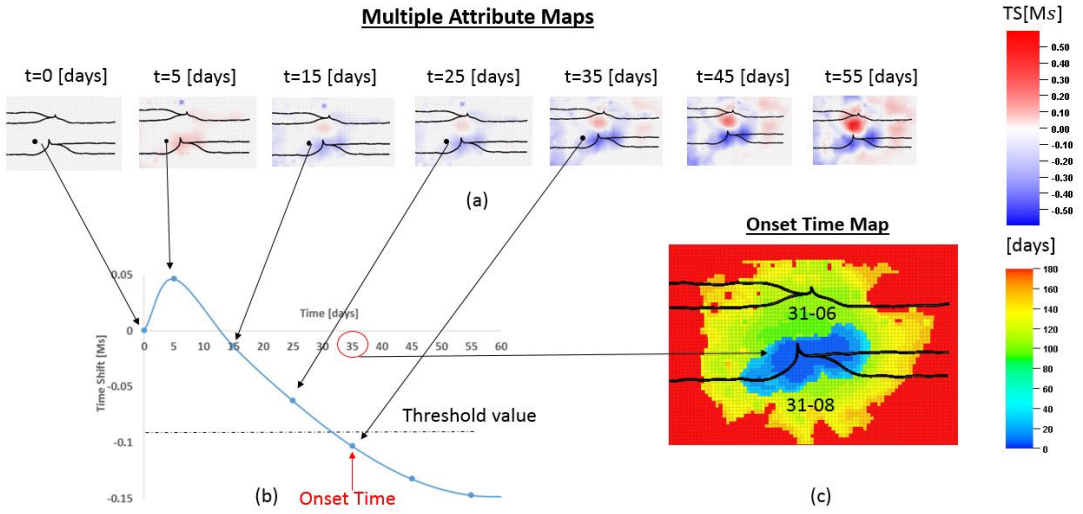

Figure 3.5 Conversion of multiple attribute maps (time shift) to onset time map. (a) A sample of 7 attribute maps (time shifts) out of 175 that are available for integration. (b) A plot of the seismic response of a specific cell (labeled as black dot in (a)) to indicate the onset time. (c) The onset time map after converting from seismic attribute to time. The contours display the steam front progression (reprinted from Hetz et al., 2017)

As mentioned earlier in section 2.1, in addition to being more efficient because of the significant data reduction, the onset time approach has the advantage of being more robust to the choice of petro-elastic model, which was used to interpret the seismic data. The following Figure 3.6 shows the comparison between the time shift maps and onset

time maps calculated with two different petro-elastic models. Clearly, many differences exist in the time shift maps, while the onset time maps are quite similar, indicating the onset time is more robust against the uncertainty in the seismic inversion results.

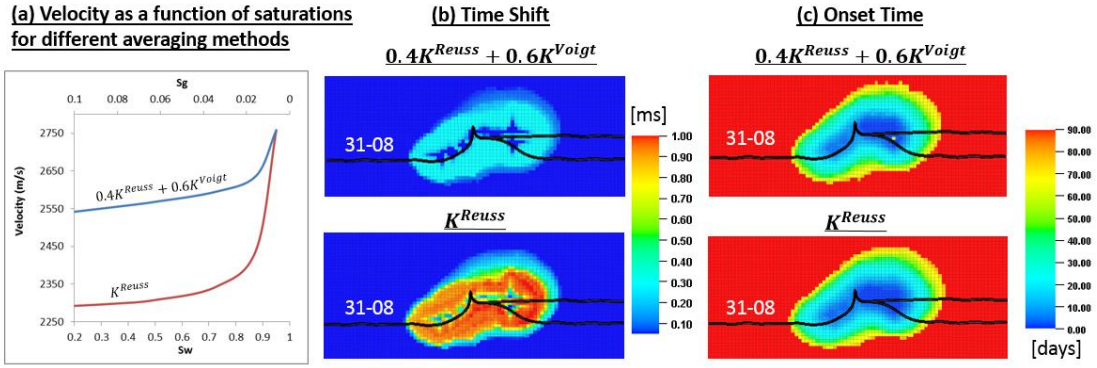

Figure 3.6 Comparison of time shift maps and onset time maps (bottom view) based on two different petro-elastic models. (a) P-wave velocity calculated with two different petro-elastic models, (b) time shift maps, (c) onset time maps. Well 31-08 is a multilateral well with 3 branches (reprinted from Hetz et al., 2017)

Based on the onset time map, Hetz et al. (2017) implemented a "Global-Local" two-step history matching workflow, successfully calibrating the reservoir permeability with better match in the bottom-hole pressure response of well 31-08.

3.1.4 Interpretation of the Time Shift Response

In this section, the causes of the change in the time shift response is discussed in detail. As shown in Figure 3.7, the change of the time shift values of the target location within the cycle of steam stimulation can be divided into 4 sections with the first 3 sections for steam injection (first 85 days) and the 4th section for production (after 90 days). For the first 5 days (first section), the time shift value increases at the beginning of the injection because of the pressure buildup before the steam chamber expands to this location. Then,

from the day 5 to day 45, the time shift value decreases resulting from the "hardening" of the formation because of the replacement of lighter gas with heavier condensed water. Then after 45 days, the time shift value became less negative because the effects of increasing pressure and temperature became dominant after the gas has been displaced or gone back to solution. Finally, after 85 days, the well started to produce and the formation "hardening" occurred again because of the pressure depletion. It is worth mentioning that the gas in the formation is the dissolved gas coming out of solution because of the pressure depletion in the previous production process.

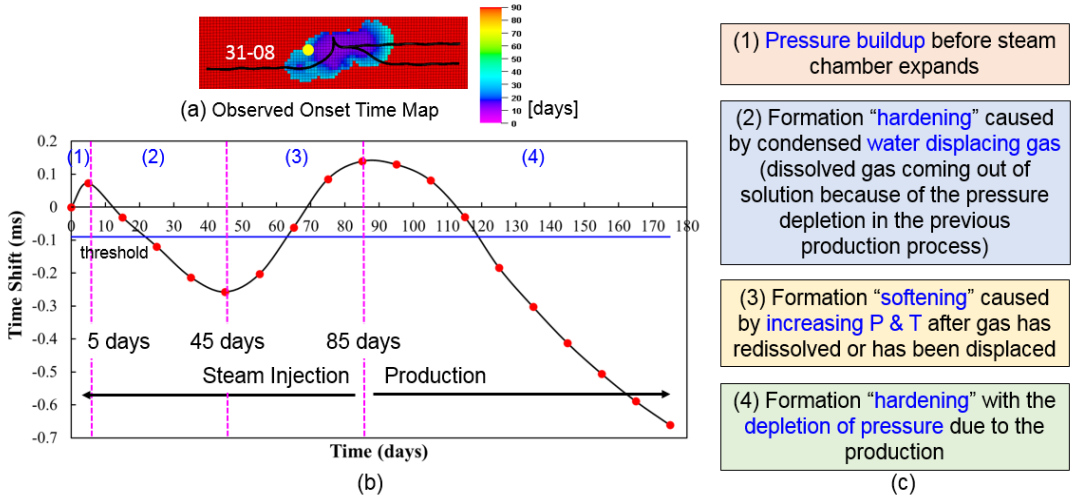

Figure 3.7 Explanation of the time shift value changing over a CSS cycle. (a) Observed onset time map (yellow point indicates the location of interest), (b) time shift values of the yellow point changing over the cycle, (c) explanation of the causes of the 4 changes

The transition in the dominant physics between section (2) and section (3) can be observed from the simulation results. The following Figure 3.8 shows the change of averaged water saturation, gas saturation, pressure and temperature of the entire column as indicated by the yellow point in Figure 3.7 (a). It can be noticed that the increases of

water saturation and the decreases of gas saturation stop after around 45 days, while the pressure and temperature increase continuously with steam injection.

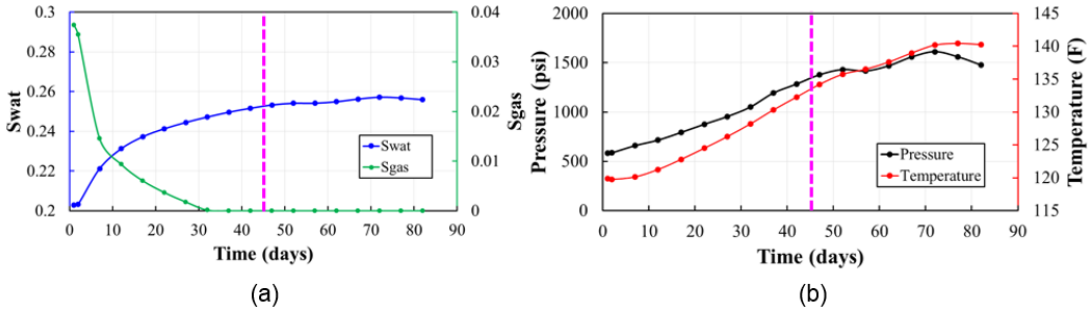

Figure 3.8 (a) Averaged water saturation and gas saturation changing over the first 85 days, (b) averaged pressure and temperature

The effects of the pressure, temperature and fluid saturations on the P-wave velocity are shown in the following Figure 3.9. By comparing the green, blue and red lines in Figure 3.9 (a) and (b), it can be seen that the saturation has the largest effect on the P-wave velocity, which is also shown in Figure 3.9 (c). In addition, with decreasing gas saturation, the effects of pressure and temperature become more significant, as can be seen from the more negative slopes of the lines in Figure 3.9 (a) and (b).

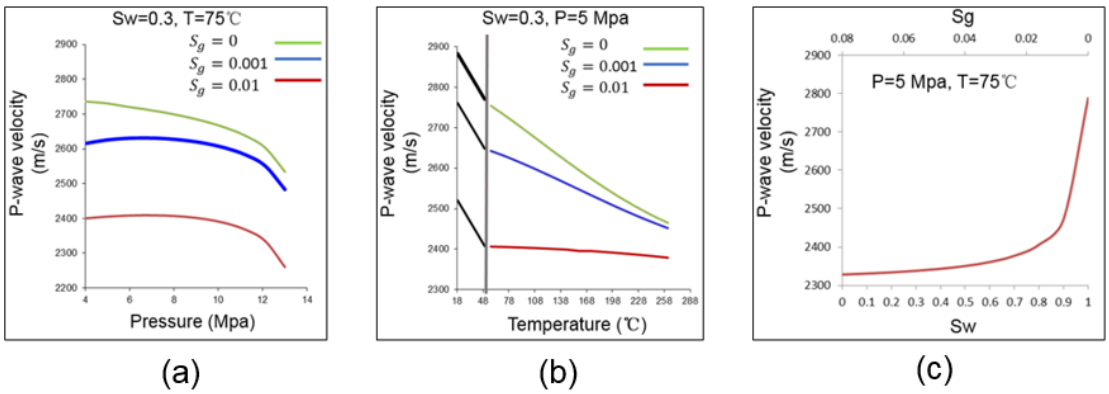

Figure 3.9 Effects of pressure, temperature and saturations on the P-wave velocity (reprinted from Hetz et al., 2017)

As mentioned earlier, the decreasing time shift values in section (2) are interpreted as the condensed water displacing the gas in the formation. This interpretation can be verified from the streamline visualizations shown in the following Figure 3.10. The displacement of gas by the condensed water can be seen clearly from the propagation of water saturation fronts and the disappearing of gas along the streamlines.

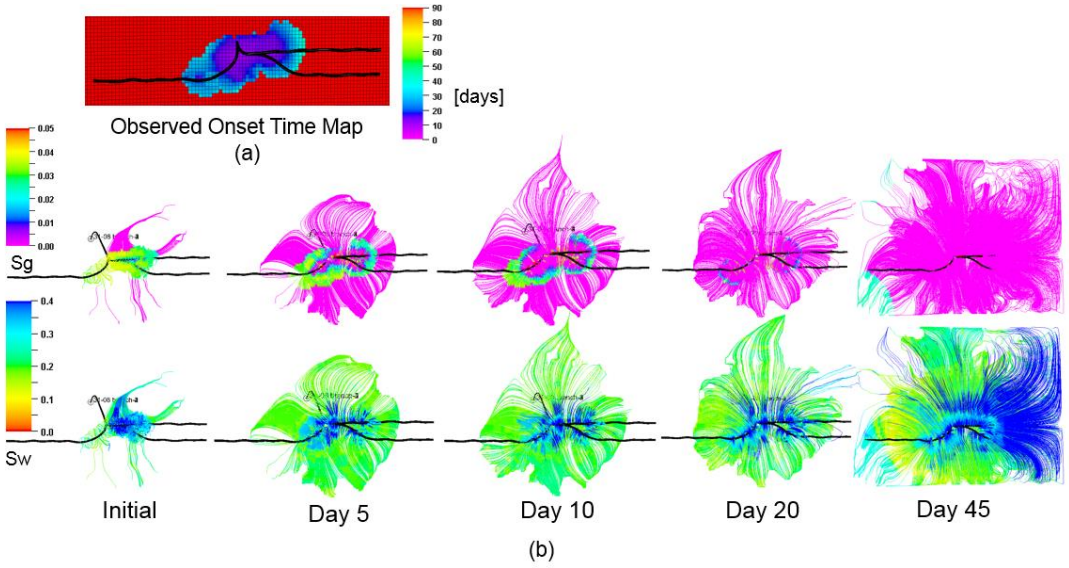

Figure 3.10 Saturations along the streamlines from the well 31-08 (multilateral well with 3 branches) show the condensed water displacing the gas. The changes of saturation contours along streamlines (b) are in consistent with the onset time map contours (a)

3.2 Sensitivity Analysis on the Impact of Seismic Survey Frequency

Vasco et al. (2015) investigated the effects of variations in seismic survey intervals on the onset time maps using a 2D synthetic case. It showed that although the truncation effect in onset time map becomes more obvious with increasing survey intervals, large-scale permeability variations can still be recovered even if the seismic surveys were spaced as much as 300 days apart. However, the results based on synthetic case may not be valid for all field cases. Because the effect of survey interval on the calculated onset time map

is affected by both the well spacing and the propagation speeds of fluid saturation fronts, which are controlled by the injection rate, fluids viscosity and formation permeability, etc. The time interval of 300 days maybe large for a reservoir with small well spacing and fast fluids propagation speed. However, it could also be a relatively small interval for a reservoir with large well spacing and slow fluids propagation speed. In this case, the effects of seismic interval on the onset time map could be compensated by the long breakthrough time or travel time of the fluids.

To further analyze the impact of seismic survey frequency on the onset time approach, sensitivity analysis is conducted based on the frequent seismic data of the Peace River case introduced above.

3.2.1 Methodology

The following Figure 3.11 shows the frequent seismic data over a targeted CSS cycle (indicated by blue rectangle in Figure 3.11 (a)). The targeted cycle contains 175 daily time shift maps over both the injection and production phase. To handle the noise contained in the data, the raw data are averaged with a 10-day smoothing window, resulting in 18 averaged time shift maps as shown in Figure 3.11 (b). The steam injection process lasted for the first 85 days, which includes the first 9 time shift maps. While the rest 9 time shift maps correspond to the soaking and production period. In this study, because we are focusing on tracking the propagation of steam front, only the first 9 time shift maps during the steam injection phase will be used for sensitivity analysis.

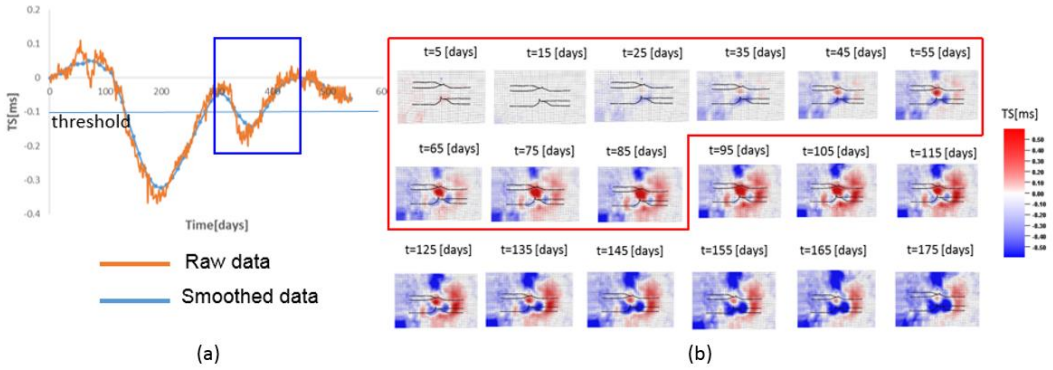

Figure 3.11 (a) A plot of the seismic response of a certain location over several CSS cycles (blue rectangle indicates the targeted cycle). (b) The 18 time shift maps after smoothing the data with 10-day averaging window. (Red polygon indicates the first 9 time shift maps for steam injection process) (reprinted from Hetz et al., 2017)

The strategy of sensitivity analysis is to compare the onset time maps calculated based on the infrequent seismic data that are sampled from the frequent seismic data (i.e. the 9 time shift maps shown in Figure 3.11 (b)). The following Table 3.1 shows the sampling schemes with increasing sampling frequency, i.e. increasing time span between consecutive seismic surveys.

Table 3.1 Sampling schemes for sensitivity analysis

Percentage of Frequent Seismic Data	Sampling Frequency (days)
100%	10
50%	20
25%	40
12.5%	80

Additionally, in order to handle the truncation effect resulted from the large time span between the seismic surveys, different interpolation methods for calculating the onset time map are compared. The following Figure 3.12 illustrate the different interpolation methods. The non-interpolation method simply takes the seismic survey time of the point

that has crossed the threshold value as the seismic onset time, while the linear interpolation method chooses the linearly interpolated time at the threshold value for a more accurate onset time value. The Lagrange interpolation method uses a higher order polynomial to approximate the seismic response change and chooses the interpolated value as the onset time. To avoid over-fitting, the number of terms included in the polynomial formulation is limited up to the point when the time shift value starts to increase. It should be pointed out that, although the non-interpolated case would not be a natural and common practice to calculate the onset time for real cases, it is still included for emphasizing the necessity of doing interpolation.

In all cases, the onset time is defined as a decrease of 0.09 ms in the time shift value, resulting from the hardening of the formation caused by the fluid substitution of initial free gas bank replaced by the injected steam/water. The threshold value is chosen based on the signal-to-noise ratio in the dataset. The initial gas bank is the dissolved gas coming out of solution because of the depletion of pressure during the previous production process.

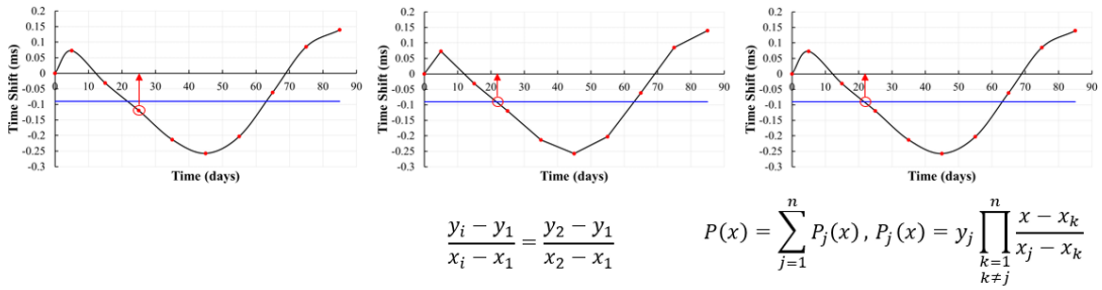

Figure 3.12 Plot of the time shift values for a certain location in the reservoir with the red arrows indicating each calculated onset time and the black lines showing the approximation of seismic response for different interpolation methods (formulas in the bottom show the linear and polynomial equation used for interpolation)

3.2.2 Results and Discussions

The following Figure 3.13 shows the calculated onset time maps with different sampling schemes and interpolation methods. It is obvious that for the case without interpolation (Figure 3.13 (a)), with less available seismic data, the truncation effect becomes more obvious. Although the overall footprint of onset time maps are about the same, the onset time pattern quickly fades away. However, with linear interpolation and Lagrange interpolation, the calculated onset time maps obtain better time resolution. In addition, even if the seismic survey intervals were increased to 4 times of that of the frequent seismic survey (from 10 days to 40 days), the calculated onset time maps (25% case) preserve much similar onset time pattern as that of frequent seismic data (100% case).

Clearly, it is shown that onset time pattern can still be extracted from the infrequent seismic data, while interpolation is required to resolve into the large time span between seismic surveys to alleviate the truncation effect and obtain an accurate onset time map.

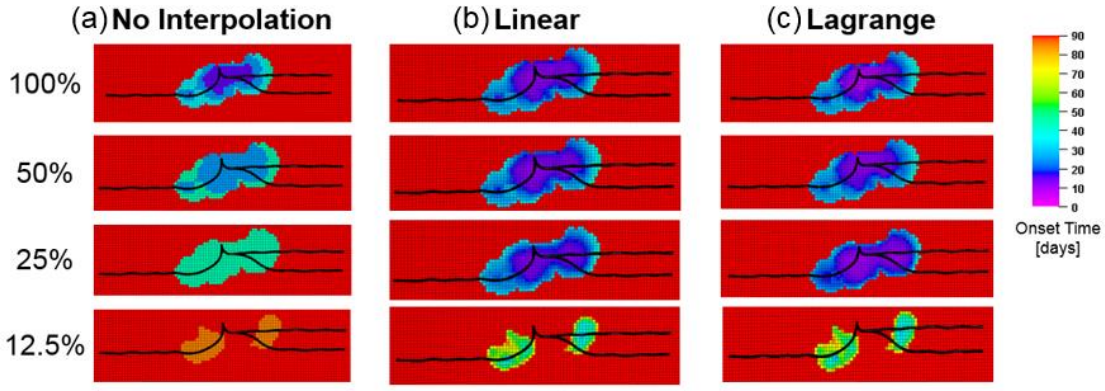

Figure 3.13 Comparison of onset time maps with different sampling schemes and interpolation methods

On the other hand, comparing the linear interpolation and Lagrange interpolation, although there are slight differences between the calculated onset time maps, both methods show comparable performance, obtaining similar onset time maps. However, the Lagrange interpolation requires more computational cost and is more difficult to implement. Moreover, it suffers from the risks of overfitting with high order terms. On the contrary, linear interpolation is much more efficient and easier to implement and is robust enough for calculating an accurate and meaningful onset time.

Additionally, it should be noticed that for cases with interpolation (Figure 3.13 (b) and (c)), the onset time maps of 12.5% case are quite different from the other cases. In this case, the onset time map does not preserve the good time resolution as that of the more frequent cases. However, it still gives some indications on the large-volume flow of injected steam through the two short perforation intervals along the west-east direction of the horizontal wellbore.

The reason why the onset time map in the last case alters much is because the change in the dominant physics is not captured in the observed seismic surveys due to the insufficient sampling. More details on the limitations of the onset time approach are discussed in section 3.4.

3.3 Interpolation vs. Non-interpolation (2D Case)

In this part, we demonstrated the necessity of doing interpolation for calculating the onset time with infrequent seismic data using a 2D synthetic case. To show the

necessity of interpolation, we compare the inversion performance based on the onset time map with linear interpolation and without interpolation.

The case studied here is a 2D synthetic case with five-spot waterflooding pattern, which is the same as the one (Figure 2.1) presented in section 2.1. The following Figure 3.14 (a) and Figure 3.14 (b) show the reference model and initial model used for inversion. The reference model is used to generate 5 sets of time-lapse seismic surveys (Figure 3.15) in the form of acoustic impedance value over a waterflooding process of 2200 days. Every two consecutive seismic surveys are either 400 or 600 days apart. Every two consecutive seismic surveys are either 400 or 600 days apart. Because the earliest water breakthrough occurs around 800 days, only two or three seismic surveys are available before the water breakthrough. Thus, the seismic surveys are relatively infrequent in time.

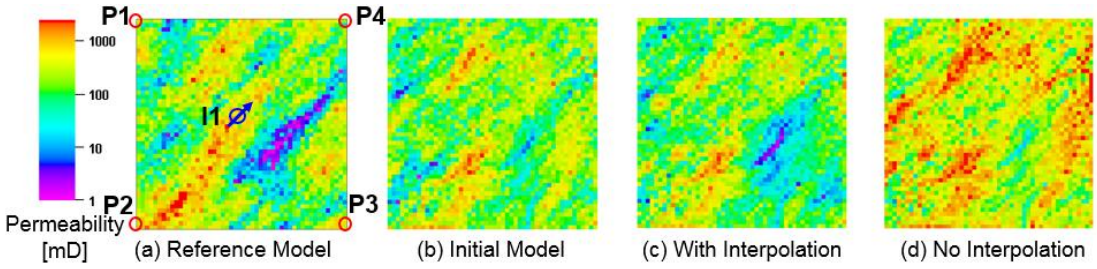

Figure 3.14 Comparison of (a) reference model, (b) initial model, (c) updated model with linear interpolation, (d) updated model without interpolation

The difference between implementing linear interpolation and non-interpolation for calculating the onset time is illustrated in Figure 3.15. The threshold value is an increase of 3% of the initial acoustic impedance value. As shown in Figure 3.15 (b), for the linear interpolation case, the calculated onset time is the interpolated time at threshold value. While for the non-interpolation case, the onset time is taken as the seismic survey

time of the point that has crossed the threshold value. In Figure 3.15 (c) and (d), clearly it can be seen that with linear interpolation, the truncation effect in the non-interpolated onset time map is alleviated. The interpolated onset time map has better time resolution than the non-interpolated onset time map, giving a more accurate representation of the propagation of the water saturation front.

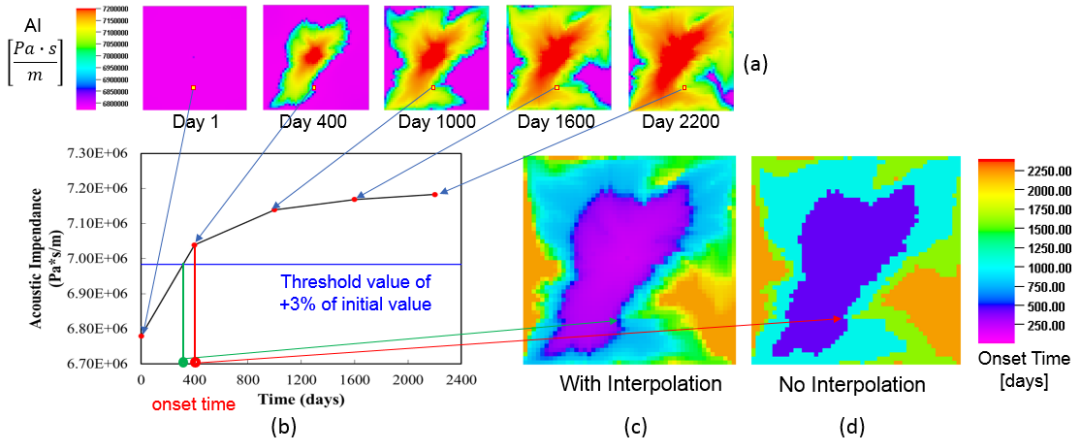

Figure 3.15 Illustration for linear interpolation and non-interpolation, (a) 5 sets of acoustic impedance maps, (b) plot of seismic response for a certain location in the reservoir (marked as yellow in (a)), (c) onset time map with linear interpolation, (d) onset time map without interpolation

To demonstrate the necessity of interpolation, onset time inversions are done separately based on Figure 3.15 (c) and Figure 3.15 (d). The inversion performance of two cases are compared. The updated models are compared as shown in Figure 3.14 (c) and (d). Comparing the updated models with the reference model, obviously, the onset time map with linear interpolation yields a much more accurate permeability update in the low permeability barrier at the right bottom corner, while the onset time map without interpolation leads to inaccurate update with overestimate in the large-scale permeability distribution. In addition, the reduction of normalized misfit shown in Figure 3.16 indicates

that the interpolated case results in the faster misfit reduction than the non-interpolated case.

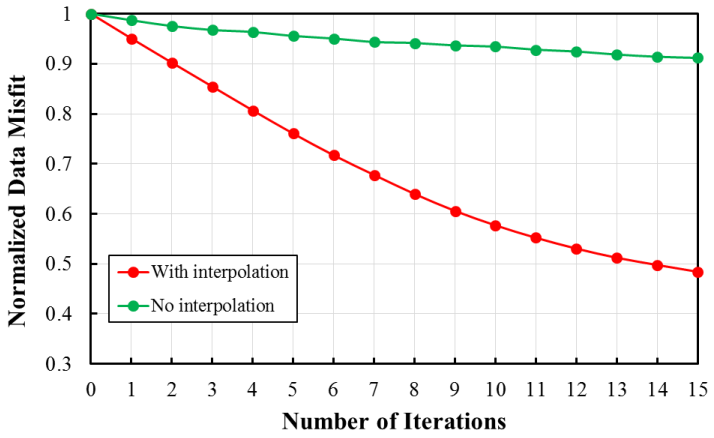

Figure 3.16 Comparison of reduction of normalized data misfit

The superior inversion performance of the interpolated case results from the denser sensitivity matrix by doing interpolation, as can be seen in Figure 3.17. The onset time sensitivity map with interpolation clearly shows the propagation of water saturation front with larger sensitivity values in the fronts and smaller sensitivity values between the fronts. However, because of the truncation effect in the non-interpolation case, the sensitivity in the non-interpolation case is much sparser. Only few of the cells in the saturation fronts have sensitivity values, which results in the inadequate model update and slow misfit reduction rate.

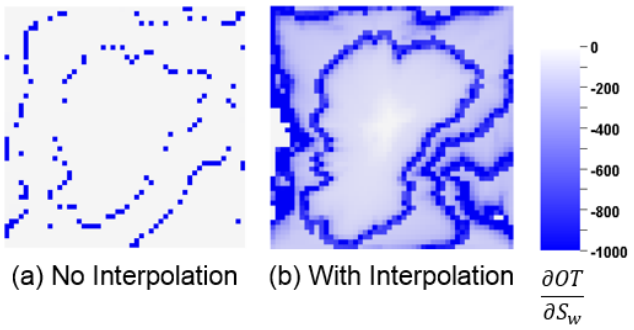

Figure 3.17 Comparison of the onset time sensitivity for linear interpolation case and non-interpolation case

The observed, initial and updated onset time maps for both cases are shown in Figure 3.18. Undoubtedly, the linear interpolation case obtains a better update and match in the onset time map than the non-interpolation case.

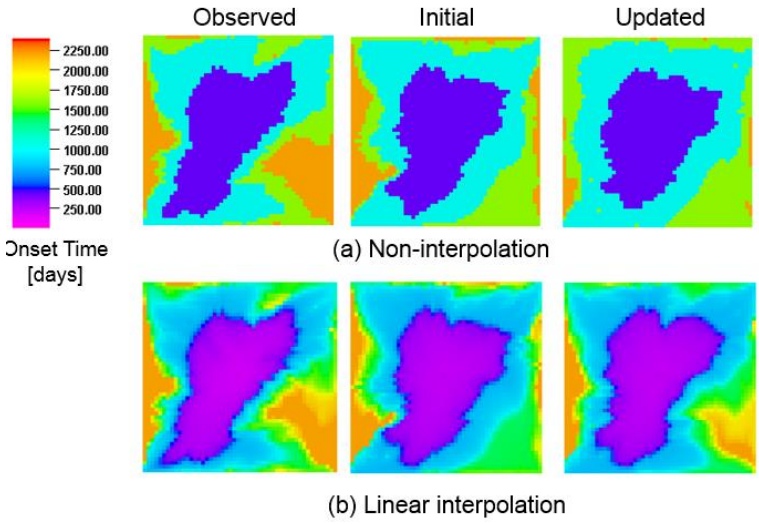

Figure 3.18 Observed, initial and updated onset time maps for (a) non-interpolation case and (b) linear interpolation case

The comparison based on the 2D synthetic case clearly indicates that the interpolation is necessary for calculating the onset time map for infrequent seismic data by resolving into the large time span between the seismic surveys, providing better time

resolution in the interpolated onset time map, yielding denser sensitivity, and leading to more accurate model update and more efficient misfit reduction.

3.4 Limitations of the Onset Time Approach

As mentioned earlier, the onset time approach has the advantages of being more efficient because of data reduction and being more robust because it is less sensitive to the choice of petro-elastic model. However, there are limitations with the onset time approach.

Vasco et al. (2015) pointed out that one of the chief drawbacks associated with the onset time approach is the temporal sampling required to resolve the onset time map. The time and expense required for conducting frequent seismic surveys prevents the onset time approach from wider use. Although in this study, the onset time approach has shown to be applicable for more infrequent seismic data with the use of interpolation, it may not work with all cases. The limitation of onset time approach for infrequent seismic data found in the sensitivity analysis is discussed in the following section.

In the sensitivity analysis in section 3.2, it is found that although the interpolated onset time maps based on infrequent seismic data (50% and 25% case) preserves the similar onset time resolution as that based on frequent data (100% case). The onset time map for the 12.5% case with the largest sampling frequency and the least seismic data alters a lot. Thus, one would like to know why the interpolated onset time map breaks. The reason why the onset time breaks is because there is a change in dominant physics within the reservoir during the injection phase, and the change is not captured by the insufficient seismic surveys with large time intervals.

A detailed analysis on the linear interpolation results with each sampling scheme is shown in the following Figure 3.19. Figure 3.19 (a) shows the observed time shift values of a certain location in the reservoir (marked with yellow circle) for all available seismic surveys during the injection phase. It can be seen that the time shift values first decrease because of the "hardening" of the formation caused by the fluid substitution of injected steam/water displacing the initial gas bank around the wellbore. Then after 45 days, the time shift values increase, resulting from the "softening" of the formation with increasing pressure and temperature after the free gas has been displaced away. The effect of the increasing pressure and temperature on the increasing time shift values was also observed and interpreted in the previous studies (Lopez et al., 2015, Przybysz-Jarnut et al., 2015, La Follett et al., 2015).

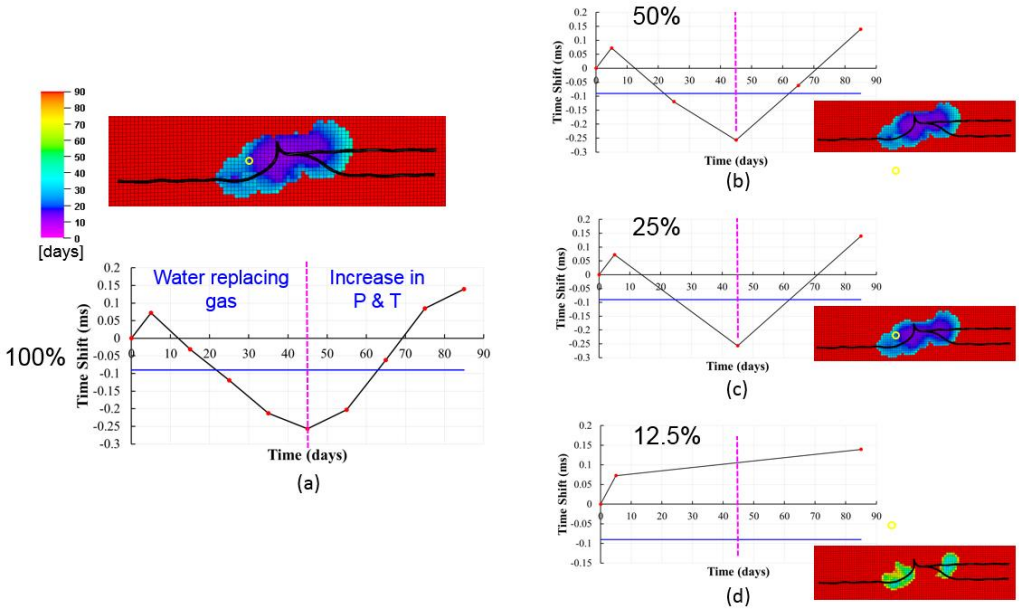

Figure 3.19 Illustration for using linear interpolation to calculate onset time for a location in the Peace River reservoir (marked by the yellow circle in the onset time map of (a)). Red points represent the available seismic data. (a) Based 100% frequent data, (b) based on 50% data, (c) based on 25% data, (d) based on 12.5% data

Figure 3.19 (b), (c) and (d) show the interpolation done with less available seismic data and the resulted onset time maps. It can be seen that for the 50% and 25% case, even with less available seismic data, the interpolated onset times for both cases are around 24 days, which is close to the 100% case. However, for the 12.5% case, with least available seismic data, the interpolation failed to find an onset time. It is because the change in the dominant physics has resulted in the change of seismic response, which was not captured in the insufficient seismic surveys. In this case, the linear interpolation fails to give a close approximation to the true seismic response.

In reality, the time at which the change in the dominant physics occurs will be affected by both the reservoir properties, such as the size of the reservoir, the change in the saturation of pore-filling fluids, etc., and the operating conditions, including the injection and production strength etc. Therefore, a detailed analysis on the petro-elastic model and reservoir conditions needs to be conducted to better understand the subsurface physics before applying the onset time approach.

In addition to the change in the dominant physics, the onset time came across difficulties in dealing with the 4D seismic data in the Norne field case, where the potential causes could be the noisy data or the inaccurate petro-elastic model or the inaccurate initial geologic model. The preliminary results are attached Appendix D.

3.5 Sensitivity Analysis on the Selection of Threshold Value (2D Case)

The choice of threshold value is critical for obtaining a clear and meaningful onset time map. In this section, the criteria for the selection of threshold value are discussed. In

addition, the sensitivity of the onset time map to the threshold value is analyzed based on a 2D synthetic case as shown in section 3.3.

3.5.1 Choice of Threshold Value

The threshold value contains two parts: the sign and the magnitude. On one hand, the sign is determined by the dominant physics within the reservoir that is being tracked. The dominant physics is the physical change in the reservoir property, such as the change of fluids saturation, pressure and temperature, etc., that has the largest contribution to the change in the reservoir seismic properties, such as the P-wave velocity or S-wave velocity. In field operation cases, there are always multiple physical phenomena happening at the same time. For example, during steam injection, the water phase saturation increases as the reservoir temperature and pressure increase. Therefore, a careful analysis on the petro-elastic model and reservoir conditions is necessary to identify the dominant physics.

On one hand, the sign of the threshold value depends on the change in the seismic signals caused by the dominant physics. In the 2D waterflooding case shown above, the average reservoir pressure does not change much because the injection and production volume are equal. Also, the reservoir temperature does not change significantly. Thus, the dominant physics is the fluid substitution of heavier injected water displacing the lighter oil, resulting in the increasing bulk rock density and therefore the increasing acoustic impedance. In such case, the sign of threshold value should be positive. On the contrary, if the injected fluid is gas rather than water, then the formation is getting “softer”, which

will lead to the decrease of bulk density and thus the decrease of acoustic impedance. Thus, the sign of the threshold value should be negative.

On the other hand, the magnitude of the threshold value is chosen based on the combined information of the magnitude of noise level in the observed seismic data and the seismic response of the undisturbed areas in the reservoir. In reality, the time-lapse seismic data are typically noisy because of the non-repeatable noise, the environmental noise, the different sensor spacing, and the changes in the near surface propagation due to variations of water table, etc. Thus, a threshold value to distinguish between the noise and the meaningful signal is critical. Additionally, the magnitude of the seismic response of the undisturbed areas in the reservoir should be considered. For example, in the waterflooding process, the seismic response of the unswept region may also change because of the increased pressure resulted from the injection. By setting the threshold value above both the noise level and the change of the seismic response of the undisturbed regions, the arrival of the dominant physics, such as the arrival of water saturation front, can be identified properly.

As mentioned by Vasco et al. (2014), there are different ways to define the onset time. For example, the onset time can be defined as the time at which the observed quantity deviates from its background value in a statistically significant manner. Alternatively, it can be defined as the time at which the change in a quantity exceeds a preset percentage of the total change of the observed quantity. Or it can be defined as the calendar time at which the rate of change of the observed quantity reaches the greatest. The optimal way to define the onset time should be the one that best characterizes the arrival of the physical

phenomenon that is being tracked. In real field applications, the definition of the onset time and the choice of threshold value would require repetitive adjustments until a clear and meaningful onset time map is obtained.

3.5.2 Methodology

To analyze the effects of threshold value on the calculated onset time map, the sensitivity analysis is conducted based on the 2D waterflooding case as presented in section 3.3. In order to analyze the effect of noise, 2% of Gaussian noise (mean of 0 and standard deviation of 0.3) are added to the observed seismic data, as shown by the scattered dots in Figure 3.20 (b). The magnitude of the noise is specified with respect to the true seismic amplitude (Figure 3.20 (a)) at a specific location for each survey. The method for adding the noise is shown in the Eq.3.2.

$$AI_{nois-added} = AI_{noise-free}(1+2\%X) \tag{3.2}$$

The X in the above Eq.3.2 is sampled from the pre-defined Gaussian distribution.

As shown in the following Figure 3.21, the noisy data of a specific location in the reservoir show some oscillation in the observed seismic amplitude curves, which may affect the calculation of the onset time value.

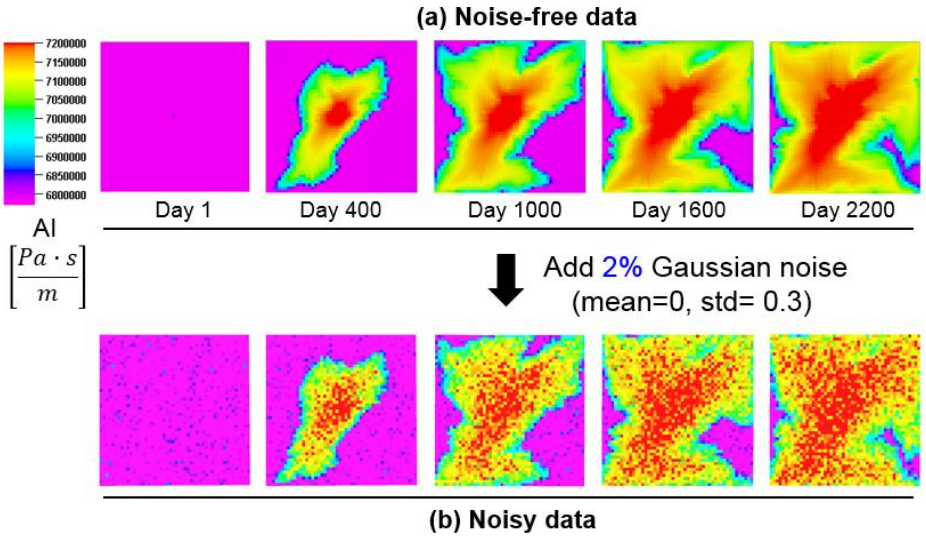

Figure 3.20 Observed seismic survey for onset time calculation. (a) Noise-free data, (b) noisy data with 2% Gaussian noise

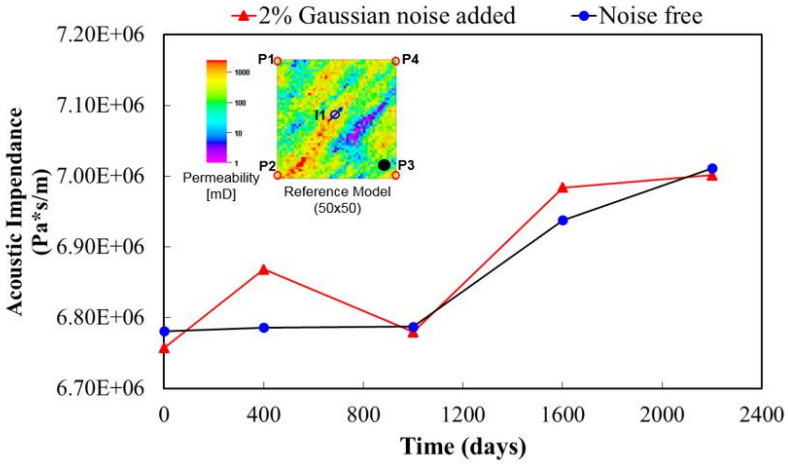

Figure 3.21 Seismic amplitude for noise free data and noisy data of a specific location in the reservoir (black dot in the permeability field)

To exam the effects of the magnitude of threshold value, three cases with different threshold values are compared as shown in the following Table 3.2. In all three cases, the threshold values are defined as a percentage increase of their corresponding initial acoustic impedance values. Case 1 has a threshold value of 0.5%, which is set below the 2% noise

level. And case 2 has a threshold value of 3% that is slightly above the noise level, while the case 3 has a relatively large threshold value of 6%, which is far above the noise level. The strategy of the sensitivity analysis is to compare the calculated onset time maps with three different threshold values for noise-free and noisy data. Since the seismic surveys are infrequent in time, linear interpolation is implemented to calculate the interpolated onset time map.

Table 3.2 Sensitivity analysis schemes

Cases	Threshold value
Case 1 < noise level	+0.5%
Case 2 > noise level	+3%
Case 3 >> noise level	+6%

3.5.3 Results and Discussions

The calculated onset time maps for all three cases with different threshold values are shown in the following Table 3.3. For the noise-free data, it can be seen that larger threshold value (6%) will lead to limited onset time pattern, as shown in the case 3. The occurrence of limited onset time pattern is because large threshold value requires large increase in the water saturation, which may not be achieved in the region that is far away from the injector by the end of the seismic surveys. Thus, a lot of areas will not yield seismic signals that cross the threshold value, leading to the unresolved onset time map. On the other hand, comparing the case 1 and case 2, it can be observed that smaller threshold value will lead to smaller onset time value, which represents the propagation of water fronts with smaller saturation. However, the onset time map of case 2 shows better

time resolution than that of case 1, as can be seen in the changing "purple" and "blue" color in case 2 comparing with the deep purple and deep blue color in case 1.

In addition, using a smaller threshold value may suffer from the risk of capturing the wrong physics that is being tracked. Taking a waterflooding case, for example the unswept region, if the reservoir pressure increases before the water arrives and the threshold value is quite small, the increasing pressure alone might cause the acoustic impedance value to increase above the threshold value. Because the pressure front travels much faster than the water saturation front, in this case, the onset time map would capture the pressure fronts rather than the water saturation fronts. This problem may be rare for infrequent seismic surveys because of the fast propagation speed of pressure fronts and the large time intervals between seismic surveys. However, it could lead to large deviation in the onset time map for frequent seismic data where the propagation of pressure fronts could be possibly captured by the frequent surveys.

Table 3.3 Onset time maps calculated with different threshold value for (a) noise-free data, (b) noisy data

Threshold value	Case 1: 0.5%	Case 2: 3%	Case 3: 6%
(a) Noise-free	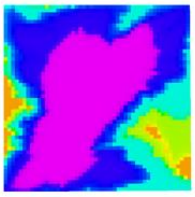	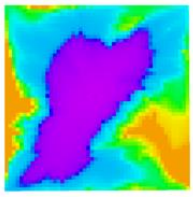	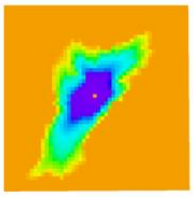
(b) 2% Gaussian Noise added	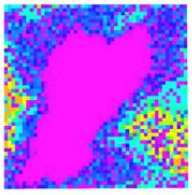	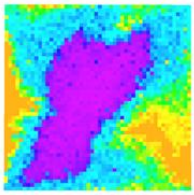	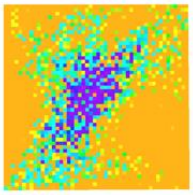

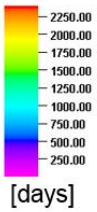

For the noisy data, the effects of noise can be clearly seen from the scattered dots in the onset time maps. By comparing the calculated onset time maps, it can be seen that the effects of noise is most significant in case 1 with the threshold value below the noise level, yielding large amount of scattered dots with inaccurate small onset time values in the onset time map. The case 2 with threshold value of 3% obtains the most clear and smoothest onset time map, where the effects of noise are greatly reduced. To obtain an even smoother onset time map, a local averaging could be applied to alleviate the effects of noise. For case 3, the limited onset time pattern is also observed as in that of the noise-free data because of the use of large threshold value.

The effects of the threshold value on the calculated onset time values are illustrated in details in the Figure 3.22. As shown in Figure 3.22 (a), because the threshold value is below the noise level, the calculated onset time based on the noisy data is much smaller than that based on noise-free data, leading to large amount of scattered dots with inaccurate onset time values. In Figure 3.22 (b), by setting the threshold value about the noise level, the effects of noise could be greatly reduced. Thus, the interpolated onset time values are pretty close. However, if the threshold value is larger than the maximum change of seismic signals, as shown in Figure 3.22 (c), no onset time could be found, leading to the limited onset time pattern. It should be noted that the differences between the noise-free and noisy initial/background values may also affect the threshold value levels, leading to the differences in the calculated onset times. However, because the noise is assumed to have a Gaussian distribution, the effects of the difference in the initial values are relative mild, thus are neglected in this study.

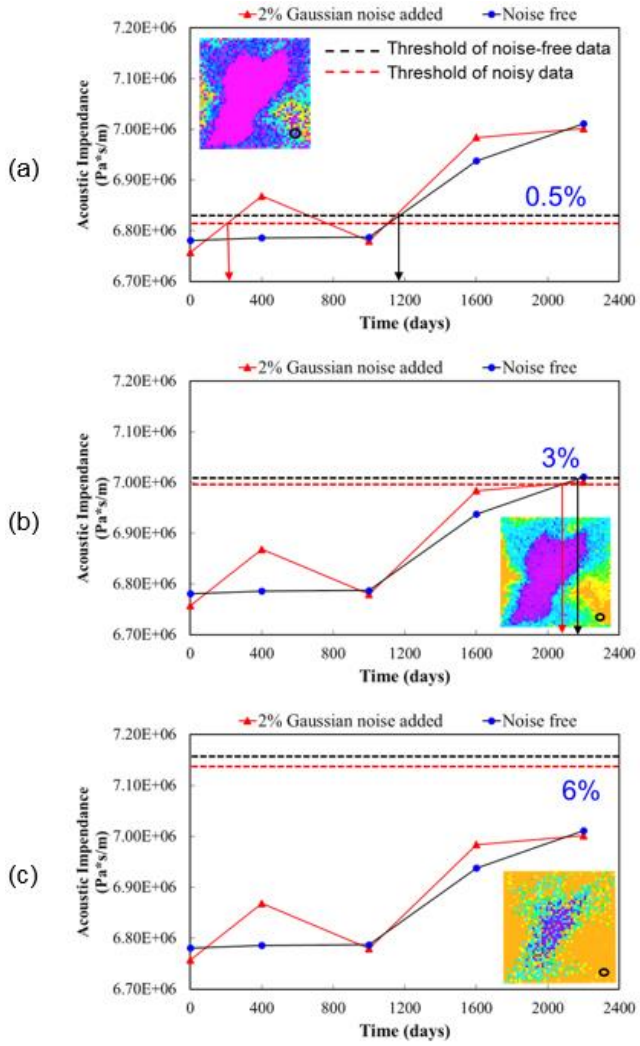

Figure 3.22 Illustration of the effects of threshold value with the acoustic impedance values of a specific location in the reservoir (black circle). (a) Case 1 with threshold value of 0.5%, (b) case 2 with threshold value of 3%, (c) case 3 with threshold value of 6%

To summarize, based on the sensitivity analysis as shown above, the threshold value should be chosen to be above the noise level to overcome the effects of noise but also below the maximum change in the seismic signals so that a meaningful and adequate onset time map could be obtained. In addition, it is worth mentioning that for frequent seismic data, since no interpolation is conducted because of the short time intervals

between seismic surveys, the effects of noise could be mostly filtered out by setting the threshold value above the noise level. This results is shown by Hetz (2017).

3.6 Summary

In this Chapter, the physical changes related to the time shift response of the Peace River case has been addressed. The applicability of the onset time approach for integrating infrequent seismic data has been validated with the sensitivity analysis on the impact of seismic survey frequency. It is shown that onset time maps extracted from infrequent seismic surveys preserve the time resolution as that extracted from the frequent seismic surveys, while interpolation is required to resolve into the large time span between seismic surveys to obtain an accurate onset time.

In addition, different interpolation methods are compared. The results show that Lagrange interpolation suffers from the risks of overfitting and is more difficult to implement. Also, it requires more computational cost. On the contrary, the linear interpolation is robust enough and more efficient and is much easier to implement. A 2D synthetic case is presented to show the necessity of interpolation. It is found that interpolation yields denser onset time sensitivity matrix, resulting in faster error reduction and more accurate model update than the case without interpolation.

Moreover, it is found that the onset time will break when the survey interval is too large and the change in the dominant physics is not captured in the acquired seismic data. In this case, the linear interpolation may not give a close approximation to the real seismic response. Thus, the onset time may not be found or may be meaningless.

Finally, the sensitivity analysis on the selection of threshold value is conducted based on a 2D case. It is shown that the threshold value should be set above the noise level to overcome the noise effects. Also, it should be smaller than the maximum change in the seismic signals to obtain a clear and adequate onset time map.

CHAPTER IV

ONSET TIME INVERSION VS. AMPLITUDE INVERSION FOR SEISMIC DATA INTEGRATION*

In this Chapter, the advantages of onset time inversion method for integrating time-lapse seismic data is explored by comparing the onset time inversion method with the traditional seismic amplitude inversion method. The inversion performance, including the accuracy of updates in the model parameter, convergence performance, and the computational time are compared. Moreover, by applying the geometric concept of nonlinearity (Bates and Watts, 1980), the nonlinearity associated with these two methods are quantitatively investigated.

The comparison is demonstrated with both 2D synthetic case and SPE Brugge Benchmark case. The 2D synthetic case involves waterflooding in a five-spot well configuration. The SPE Brugge Benchmark case involves waterflooding in a large field-scale development. Part of the results have been presented in the previous work (Liu 2018). In this thesis, the emphasis has been placed on comparing the inversion performance of the two inversion methods.

* Part of this section is reprinted with permission from "Seismic Onset Time Inversion Method for Infrequent Seismic Surveys" by T. Liu, 2018. Paper 1940440 prepared for presentation at the SPE Annual Technical Conference and Exhibition held in Dallas, Texas, USA, 24 September –26 September.

4.1 Onset Time Inversion and Amplitude Inversion

As mentioned in section 2.3, the seismic inversion workflow often requires solving the minimization problem of the objective function, through which the model parameter, such as the permeability is updated to match the simulated seismic response with the observed seismic response. The traditional seismic amplitude inversion method aims at matching the seismic amplitude (or the change in the amplitude) of multiple surveys, while the onset time inversion method focuses on matching a single onset time map. The following Figure 19 shows the comparison between the amplitude matching and onset time matching. The amplitude inversion method is based on shifting the seismic response curves vertically to match the seismic amplitude, while the onset time inversion method is based on shifting the seismic response curves horizontally to match the travel time of the fluid saturation front.

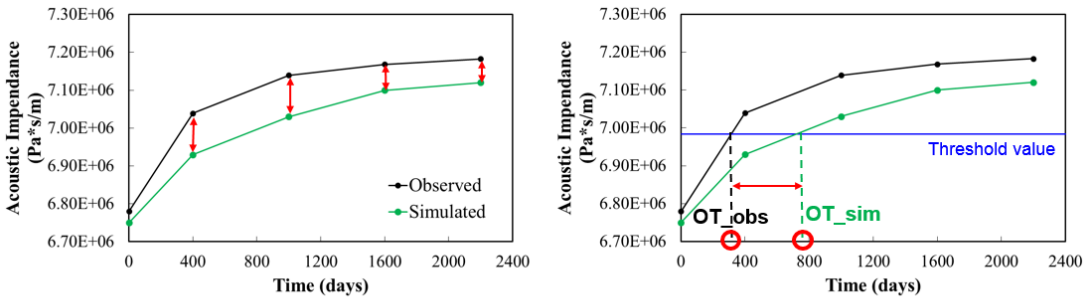

(a) Amplitude matching (b) Onset time matching

Figure 4.1 Illustration for amplitude inversion and onset time inversion. (a) Amplitude matching, (b) onset time matching.

The advantages of travel-time inversion methods are documented in the geophysics literature. Luo and Schuster et al. (1991a and 1991b) showed that travel-time inversion has the quasi-linear properties as opposed to the amplitude inversion method,

which can be highly nonlinear. Cheng et al. (2005) compared the travel-time inversion method with the amplitude inversion method for production data integration. He showed that the travel-time inversion method is more linear than the amplitude inversion method by several orders of magnitude, leading to its superior convergence performance.

4.2 Measurement of Nonlinearity

Characterizing and assessing the nonlinearity of the inverse problem helps to gain insight about the robustness and efficiency of seismic data integration approaches. In this study, the degree of nonlinearity associated with the onset time inversion and seismic amplitude inversion method are quantitatively investigated.

The nonlinearity is measured using the geometric concept put forward by Bates and Watts (1980). Grimstad and Mannseth (2000) used this method to investigate the relationship between the nonlinearity, the scale, and the sensitivity in parameter-estimation problems. Cheng et al. (2005) applied this measure to examine the nonlinearities in travel-time and amplitude inversion for production data integration. In this study, the measure of the curvature of the outcome locus is used to quantitatively measure the nonlinearities in the onset time and amplitude inversion method for seismic data integration.

If the seismic response is given by F , then the measure of the curvature is given by

$$\kappa = \frac{\| F_{mm} \|}{\| F_m \|^2}. \tag{4.1}$$

The F_m is the vector of the first-order derivatives of the seismic response F with respect to the parameter vector m, and F_{mm} is the vector of the second-order derivatives. As shown in the following Figure 4.2, the nonlinearity κ represents the inverse of the radius of circle that best approximates the outcome locus F in the direction of F_m at m. Therefore, a large nonlinearity will be represented as a small radius and large curvature in the outcome locus.

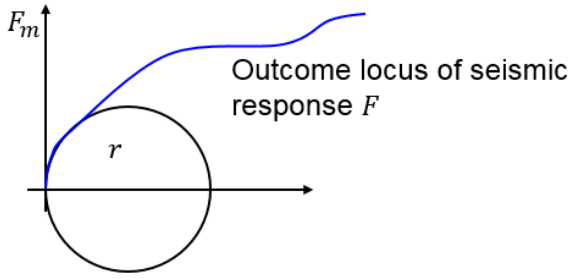

Figure 4.2 Geometric meaning of the measure of nonlinearity (reprinted from Bates et al., 1980)

Bates and Watts (1980) separate the nonlinearity measures into the parameter-effect curvature and intrinsic curvature. Thus, they decompose the second-order derivative F_{mm} into one component parallel to the tangent plane defined by F_m for all directions and another component normal to that plane. Here, the tangent vector F_m and the second-order derivative F_{mm} are essentially obtained from the sensitivity calculations. The sensitivity of the onset time inversion method is discussed in details in section 2.5, and it is given as

$$G_{OT} = \left(\frac{\partial OT}{\partial k_1}, \frac{\partial OT}{\partial k_2}, ..., \frac{\partial OT}{\partial k_n} \right)^T . \tag{4.2}$$

The seismic amplitude sensitivity is calculated in the similar way by adding a perturbation, which is given by

$$G_{AI} = \left(\frac{\partial AI}{\partial k_1}, \frac{\partial AI}{\partial k_2}, ..., \frac{\partial AI}{\partial k_n} \right)^T . \tag{4.3}$$

To account for the variation in the units, we need to normalize the parameters or use a linear transformation to obtain a meaningful solution. Simply expressing the parameters in the original units can be a bad choice because parameters of different types can be of different numerical orders (Duijndam 1988a, 1988b). There are several options to achieve a meaningful solution: (1) to express the parameters in units that correspond to the parameter ranges of interest for the problem; (2) to take the a priori standard deviations as units; and (3) to statistically normalize the parameters with the transformation so that the transformed parameters have the identity matrix as a priori covariance matrix. Here the option 3 is used to express the tangent vector F_m and second-order derivative F_{mm}.

The tangent vector F_m can be calculated with the following Eq. 4.4.

$$F_m = \left[\frac{J_y}{J_x} \right] = -\left[\frac{C_n^{-\frac{1}{2}} G}{C_x^{-\frac{1}{2}}} \right] \tag{4.4}$$

G is the sensitivity matrix, C_n is the data covariance and C_x is the parameter covariance. The second-order derivative F_{mm} can be written as the sum

$$F_{mm} = H_x + H_y . \tag{4.5}$$

The H_y is the contribution from the data, which can be calculated by

$$H_y = J_y^T J_y . \tag{4.6}$$

And H_x is the contribution from the prior information, which can be calculated by

$$H_x = J_x^T J_x = C_x^{-1}. \tag{4.7}$$

By statistically normalizing the F_{mm} with $D = C_x^{\frac{1}{2}}$, we have

$$F_{mm} = D^T (H_x + H_y) D = C_x^{\frac{1}{2}} H_y C_x^{\frac{1}{2}} + I. \tag{4.8}$$

With Eq.4.4 and Eq.4.8, the nonlinearity can be calculated using Eq.4.1. In this study, the spatial nonlinearities for each iteration of onset time inversion and amplitude inversion are calculated and the maximum spatial nonlinearities for each iteration are compared.

4.3 2D Five-spot Case

4.3.1 Case Introduction

The comparison between the onset time inversion and amplitude inversion is first done with the 2D synthetic case. The 2D case involves a five-spot waterflooding pattern with one central injector and four corner producers. The reference model and initial model used in this case are shown in Figure 4.3 (a) and (b) respectively. The reservoir model parameters are listed in Table 4.1. The reference model is used to generate the 5 sets of observed seismic data to be used for seismic inversion. The observed seismic data shown in Figure 4.4 is the acoustic impedance of reservoir formation. Every two seismic surveys are either 400 days or 600 days apart. Because the water breakthrough time ranges from around 500 days to 1000 days, only around two seismic surveys are available before water breaks through. Thus, the seismic surveys are considered as infrequent in time.

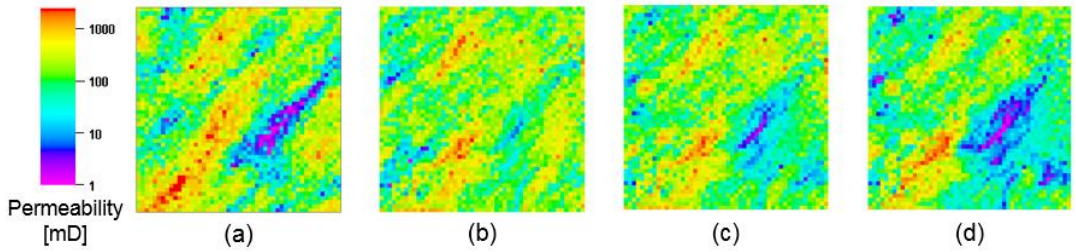

Figure 4.3 Permeability of (a) reference model, (b) initial model, (c) onset time updated model, (d) amplitude updated model (reprinted with permission from Liu et al., 2018)

Table 4.1 Model parameters in 2D synthetic case (reprinted with permission from Liu et al., 2018)

Grid number	50 x 50 x 1
Grid size	60 ft x 60 ft x 10 ft
Wells location	I1(25,25,1), P1(1,1,1), P2(1,50,1), P3(50,50,1), P4(50,1,1)
Injection rate	2500 bbl/day
Producer BHP	629 psi

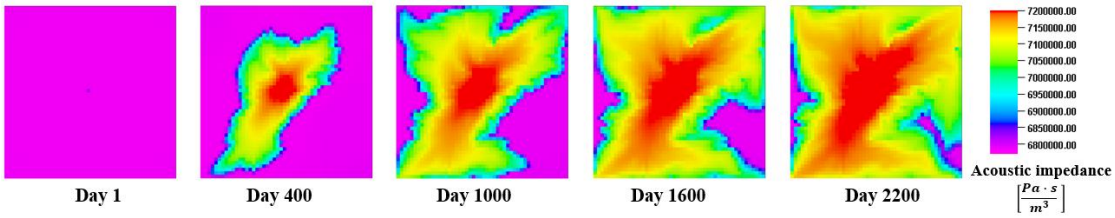

Figure 4.4 Observed seismic data generated with the reference model at 5 different survey times (reprinted with permission from Liu et al., 2018)

By imposing a threshold value of an increase of 3% of the initial value, the observed onset time map is obtained as shown in Figure 4.5 (a). The observed onset time map clearly shows the preferential propagation of water saturation front along the west-south and east-north directions, implying the underlying fast flow channels in these directions. The fast flow channels can be validated by the high permeability flow path along the diagonal as shown in the reference model (Figure 4.3 (a)).

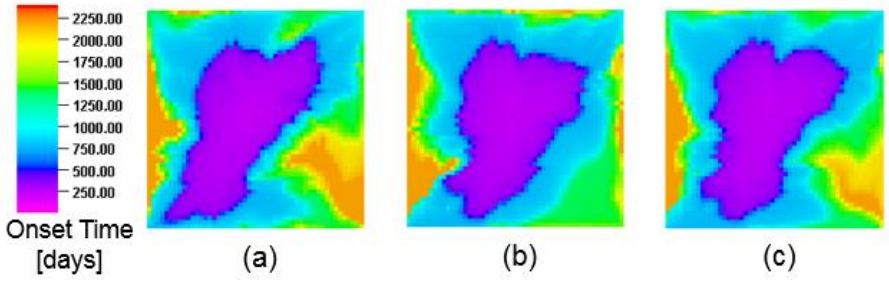

Figure 4.5 Seismic onset time map, (a) observed, (b) initial, (c) updated (reprinted with permission from Liu et al., 2018)

4.3.2 Onset Time Matching vs. Amplitude Matching

The objective of this case study is to compare the inversion performance of the onset time matching method with the traditional amplitude matching method. In this synthetic case, the onset time inversion is based on matching a single onset time map while the amplitude inversion method is based on matching 4 sets of amplitude change maps sequentially. The onset time inversion was run for 15 iterations. The amplitude inversion was run for 15 iterations for each of the 4 sequential inversions, which adds up to 60 iterations in total. The model update, convergence performance, and CPU time were compared. In addition, the nonlinearity associated with these two methods were quantitatively investigated.

The updated models are shown in Figure 4.3. It can be seen that both the onset time updated model and amplitude updated model recover the low permeability barrier at the bottom right corner. As shown in Figure 4.6, both the updated models give better water cut predication than the initial model. For example, in the producer 3, the rise in the water cut is delayed because of the recovered low permeability barrier in the bottom right corner.

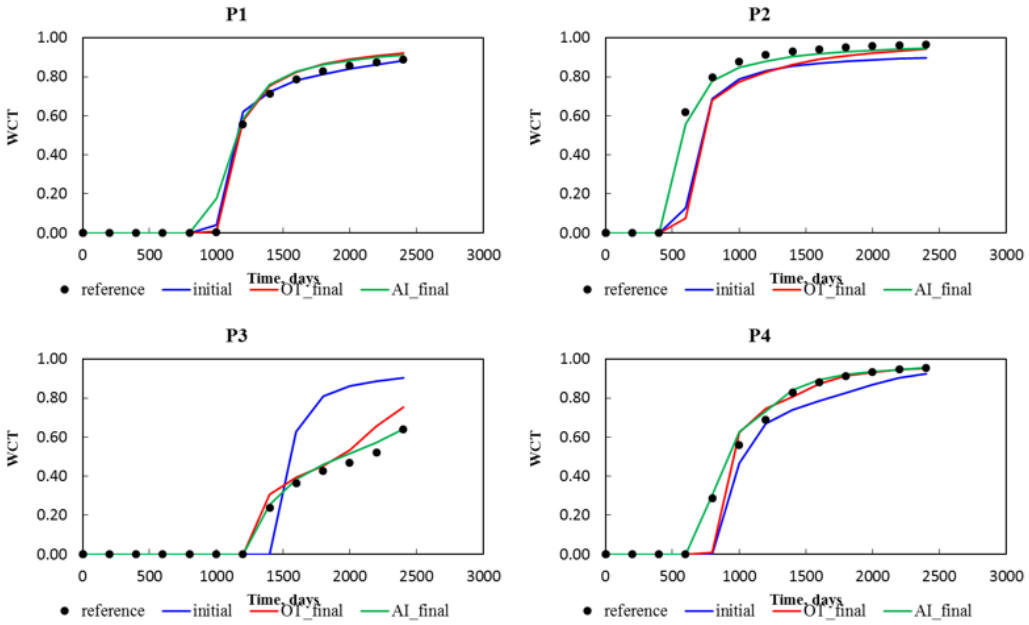

Figure 4.6 Updated models yield better water cut predication for 4 producers (black dots-initial, red-onset time updated, green-amplitude updated)

Although both methods give comparable permeability update, the onset time method is more efficient than the amplitude inversion method. The following Figure 4.7 shows the comparison of the reduction of normalized data misfit and computational cost (CPU time) between these two methods. The convergence speed is affected by both the nonlinearity of the problem and the choice of damping and smoothing factors in the numerical algorithm (LSQR) used to solve the minimization problem. In order to obtain a fair and meaningful comparison, the sensitivity matrix and data misfit vector for these two methods are normalized with the maximum absolute misfit value, and the damping and smoothing factor are chosen to be 1 for both cases.

The results show that the onset time has overall superior convergence performance than the amplitude inversion method. Moreover, the CPU time of onset time inversion

method is around 4 times less than that of the amplitude inversion method. This is because the onset time method matches a single onset time map, while the amplitude inversion method matches 4 sets of amplitude maps sequentially. The update in the onset time map can be seen in Figure 4.5, and the update in the acoustic impedance change maps are shown in Figure 4.8.

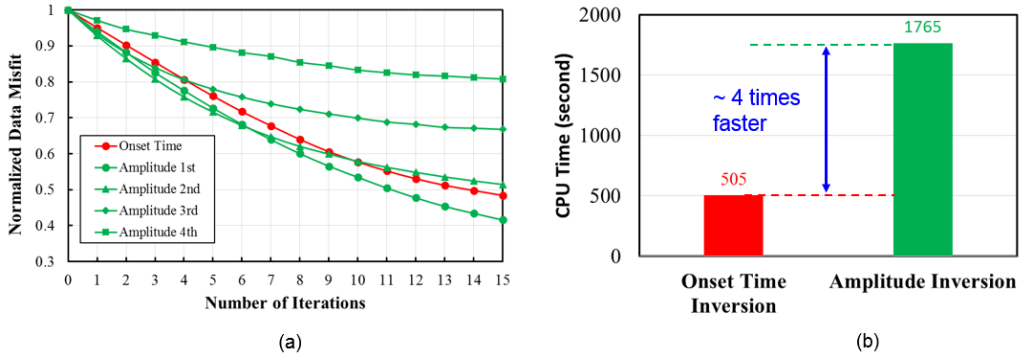

Figure 4.7 Comparison of inversion performance, (a) reduction of normalized data misfit, (b) CPU time

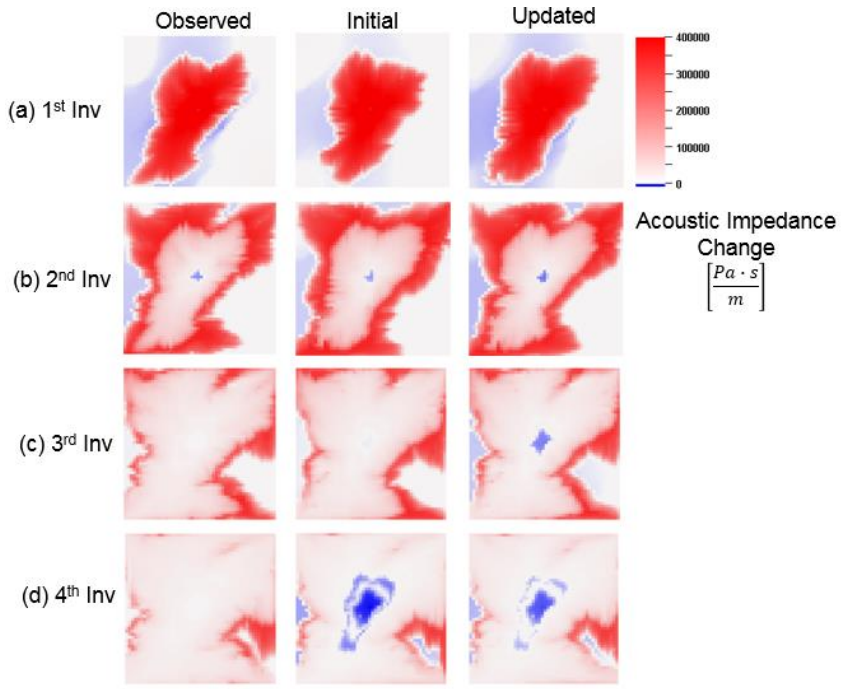

Figure 4.8 Update in each set of acoustic impedance change maps

The superior convergence performance of the onset time inversion method can be attributed to the quasi-linear properties of the travel-time matching method. The spatial nonlinearity of the last iteration of these two methods are compared in the following Figure 4.9. In addition, the maximum nonlinearity value for each iteration are compared in Figure 4.10. Clearly, it can be seen that the nonlinearity of onset time inversion method is not only much sparser in space but also much smaller in magnitude than that of the amplitude inversion method. In Figure 4.10, it shows that the onset time is more linear than the amplitude inversion method by 6~7 orders of magnitude.

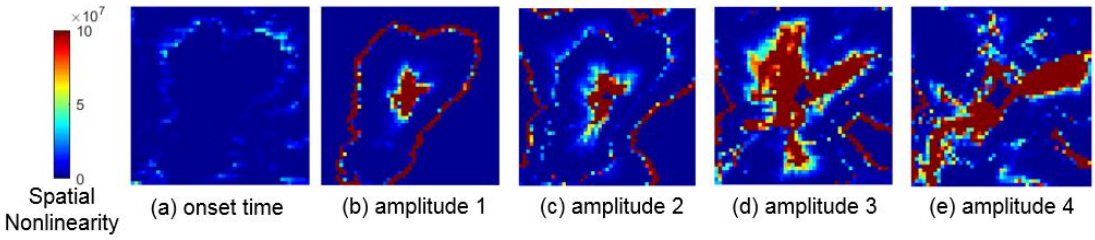

Figure 4.9 Comparison of the spatial nonlinearity of last iteration, (a) onset time inversion, (b) to (e) amplitude inversion of the first to fourth AI change map respectively

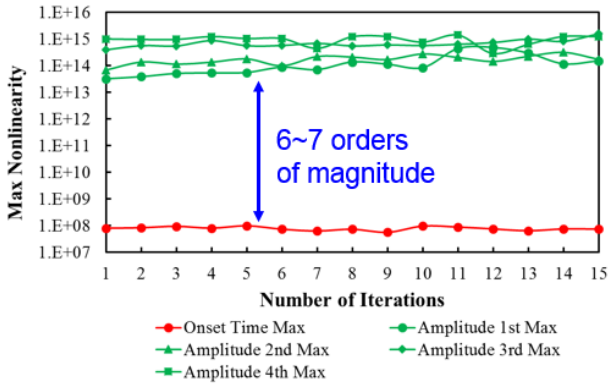

Figure 4.10 Comparison of the maximum nonlinearity of each iteration

The smaller nonlinearity of the onset time inversion method can be attributed to the attractive quasi-linear properties of travel-time matching method. The advantages travel-time inversion method are well documented in the context of seismic inversion (Luo and Schuster et al., 1991a and 1991b; Zhou et al., 1995). Luo and Schuster et al. (1991b) has discussed about the merits of working with the skeletalized data rather than raw data. The skeletalized data is defined as a reduced data set derived from the original data which retains the important information about the model parameter of interest. Luo and Schuster et al. (1991a and 1991b) has shown that the skeletalized data (such as the travel-time or seismic onset time) may be strongly influenced by only one type of model parameter (for

example, the fluids saturation) and lead to a quasi-linear misfit function. However, the raw data (such as the seismic amplitudes) could be significantly affected by multiple types of model parameters, which results in highly non-linear misfit function. As a result, the amplitude matching method has poorer convergence performance and can easily get stuck in local minima during the minimization process of misfit function, if the starting model is moderately far from the actual model.

The sparser onset time nonlinearity as opposed to the amplitude nonlinearity results from the sparser onset time sensitivity as compared with the amplitude sensitivity. The comparison of the onset time sensitivity and amplitude sensitivity of last iteration are shown in Figure 4.11. Obviously, the onset time sensitivity is more focused on the saturation front, while the amplitude sensitivity is more diffused over the entire region.

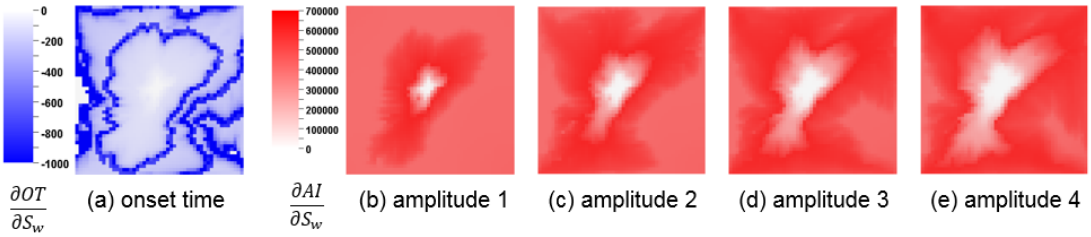

Figure 4.11 Comparison of the sensitivity of last iteration, (a) onset time sensitivity, (b) to (e) amplitude sensitivity of the first to fourth amplitude inversion

4.4 Brugge Benchmark Case

4.4.1 Introduction of Brugge Case

The Brugge field model was designed for a SPE benchmark project to test the combined use of history matching and waterflooding optimization workflow (Peters et al., 2010). It consists of more than 60,000 cells. It is a typical North Sea Brent-type reservoir, consisting of 4 primary formations: Schelde, Mass, Waal and Schie. The structure of

Brugge field shown in Figure 4.12 consists of an east/west elongated half-dome with a large boundary fault at its northern edge and one internal fault with a modest throw at an angle of approximately 20° to the boundary fault at the northern edge. The dimensions of the field are roughly 10 km × 3 km. The reservoir model represents an undersaturated oil reservoir undergoing waterflooding development. There are 20 producers locating on the top of the dome within the oil-rich region. 10 peripheral water injectors provide pressure support in addition to the aquifer. The injection rate is 10,000 bbl/day and the producers are constrained with a liquid production rate of 5,000 bbl/day.

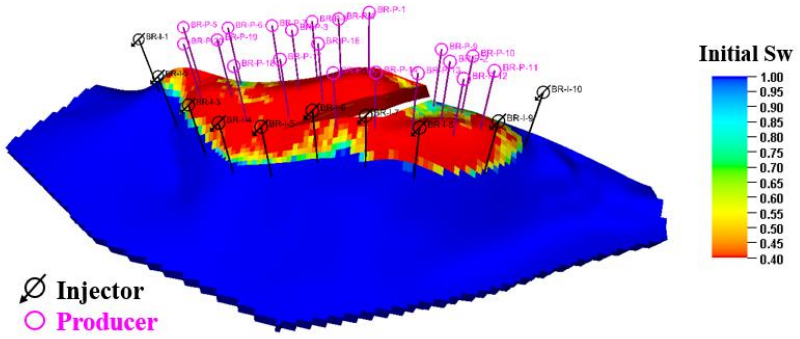

Figure 4.12 Initial water saturation of Brugge model with blue color showing the bottom aquifer and red color showing the oil in the top of the dome (reprinted with permission from Liu et al., 2018)

A total of 104 realizations were generated by four classes of geologic control parameters: (1) facies association, (2) facies modeling, (3) porosity, and (4) permeability. The detailed description of the realizations of reservoir properties can be found in Peters et al. (2010). Two realizations are chose to be the reference model (realization 103) and the initial model (realization 67). The two models have large-scale permeability difference as can be seen in Figure 4.13.

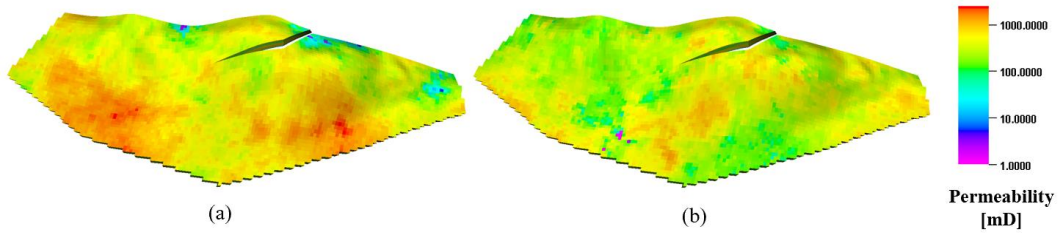

Figure 4.13 (a) Reference model (realization 103), (b) initial model (realization 67) (reprinted with permission from Liu et al., 2018)

The reference model is used to generate the observed seismic data every year since the beginning of the waterflooding process. Because the earliest water breakthrough time occurs around 1000 days, only two or three seismic "snapshots" of the reservoir are available before the water breaks through into the producers. Thus, the observed seismic surveys are considered relatively infrequent in time.

The observed acoustic impedance maps are shown in Figure 4.14. It can be noticed that the dome has lower acoustic impedance values compared with the aquifer, because the dome is rich in the "softer" fluid, oil, which has a lower density than the water. Using a threshold value of an increase of 0.8% of initial acoustic impedance value, the interpolated onset time map is obtained as shown in Figure 4.15.

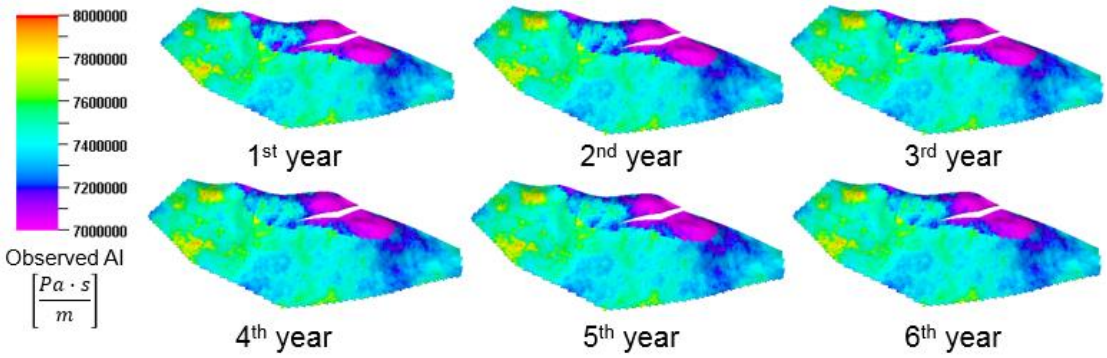

Figure 4.14 Observed acoustic impedance (layer 7) maps generated with reference model for 6-year waterflooding process (reprinted with permission from Liu et al., 2018)

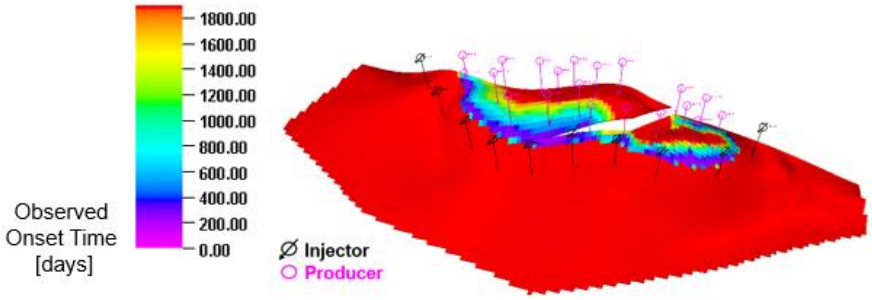

Figure 4.15 Observed onset time map (layer 7) (reprinted with permission from Liu et al., 2018)

4.4.2 Onset Time for Efficient Reservoir Imaging

It should be emphasized that the onset time is not only more robust and more efficient, but also is a great tool for efficient reservoir imaging and dynamic reservoir management. Figure 4.14 shows the acoustic impedance maps over the six-year waterflooding history. One can hardly notice the change in the acoustic impedance maps as the water front moves upwards to the producers. However, in the onset time map (Figure 4.15), the encroachment of the aquifer or the movement of the water saturation front is clearly shown in the onset time map with different color indicating the different arrival time of water saturation front.

As mentioned earlier in section 2.1, the onset time represents the travel time of water from a starting point (injector or aquifer) to a certain location. The physical meaning of the onset time can be more directly illustrated by overlapping the onset time map with the streamline trajectories before and after the waterflooding (Figure 4.16). The streamlines are generated with in-house software by post-processing the cell flux obtained from the forward simulation. The blue lines show the streamline trajectories from the injectors to the producers. By applying a cutoff of 0.45 water saturation, the cut-off edge

of streamlines defines the location of the 0.45 water saturation front. The yellow line, which lies in the lower edge of the onset time map in Figure 4.16 (a), shows the initial water saturation front at the beginning of waterflooding. The black line, which lies in the upper dome in Figure 4.16 (b), shows the final water saturation front after a 6-year waterflooding process. The water saturation fronts consistently align with the onset time map, proving the efficacy of onset time map for representing the propagation of water saturation front.

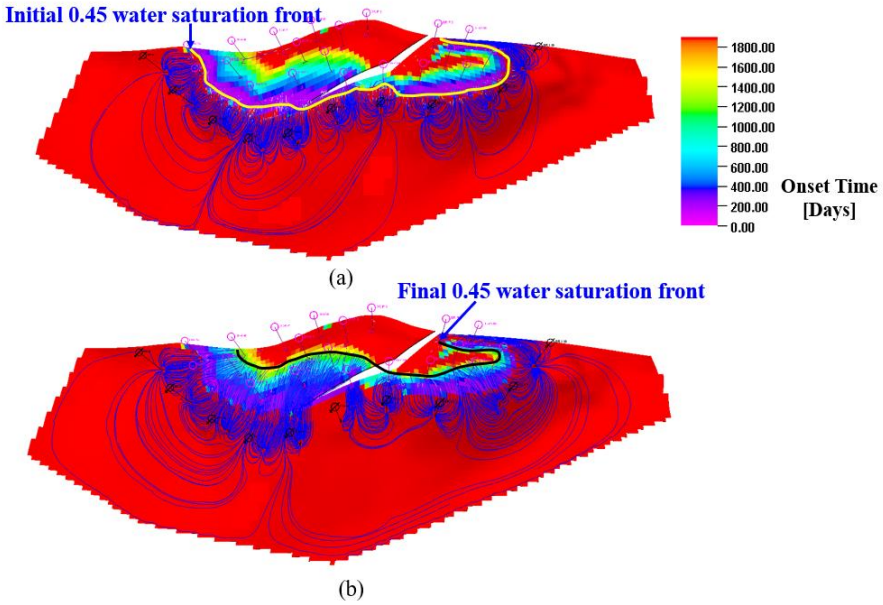

Figure 4.16 Streamlines (blue lines) overlapped with onset time map (layer 7), (a) the yellow line shows the location of initial water saturation front, (b) the black line shows the location of final water saturation front (reprinted with permission from Liu et al., 2018)

Figure 4.17 shows the onset time map at each layer corresponding to the 4 different types of formation. It can be observed that the onset time pattern is more obvious in the Schelde and Waal formations than in the Mass formation, because water preferentially flows into these high permeability formations. The onset time map in the Schelde

formation has a smaller onset time pattern than the Waal formation, because the Schelde formation is located on the top of the dome. Due to the gravity effect, most of the water tends to flow into the high permeability Waal formation with lower altitude. The Schie formation, which is at the bottom of the reservoir has no onset time pattern, because this formation contains the bottom aquifer and has been initially filled with water. There is no change in the water saturation, leading to minor change in the seismic response. Therefore, no seismic signals have crossed the threshold value, and thus no onset time can be found.

The difference in the onset time map for each layer clearly shows the invasion of water in different formation, demonstrating the advantages of onset time approach for efficient reservoir imaging and dynamic reservoir management.

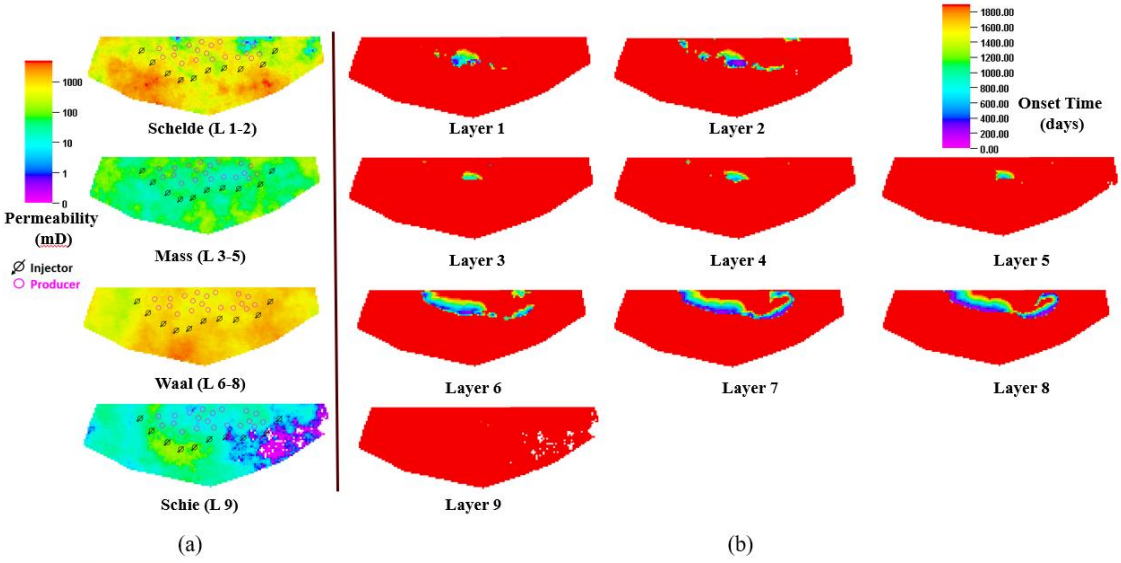

Figure 4.17 Onset time map at each layer shows the invasion of water, (a) average permeability for each type of formation, (b) onset time maps for each layer (reprinted with permission from Liu et al., 2018)

4.4.3 Onset Time Matching vs. Amplitude Matching

The objective of this case study is to compare the inversion performance of onset time inversion method based on a single onset time map (Figure 4.15) with the amplitude inversion method based on 5 acoustic impedance change maps. The 5 sets of acoustic impedance change maps are the differences between every two consecutive acoustic impedance maps. The model update, convergence performance, and CPU time are compared. Additionally, the nonlinearity associated with these two methods are quantitatively investigated.

The permeability updates for selected layer 7 are shown in the following Figure 4.18. The updates in the model via onset time inversion and amplitude inversion are found to be similar. It can be seen that most of the permeability updates locate along the main flow path within the swept region, owing to the use of streamline-based sensitivity. In addition, both the onset time and amplitude method obtain similar permeability update as the permeability change required, which can be noticed from the "red-blue spatial pattern" highlighted in the black circles. The permeability updates of both methods for each layer are shown in Figure 4.19, where the high permeability channels and low permeability barriers are recovered along the main flow paths.

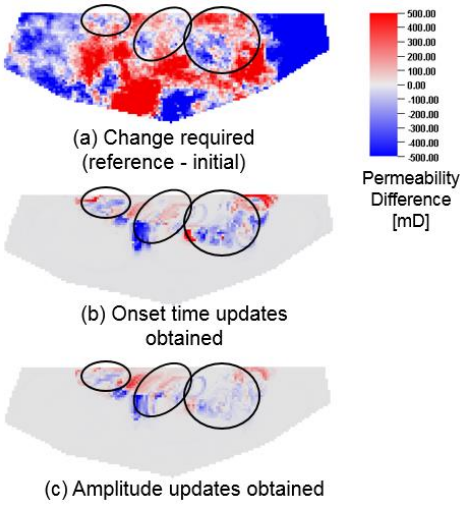

Figure 4.18 Comparison of permeability change (layer 7) with black circles indicating areas with similar permeability updates, (a) change required (reference - initial), (b) onset time updates obtained (onset time updated - initial), (c) amplitude updates obtained (amplitude updated - initial) (reprinted with permission from Liu et al., 2018)

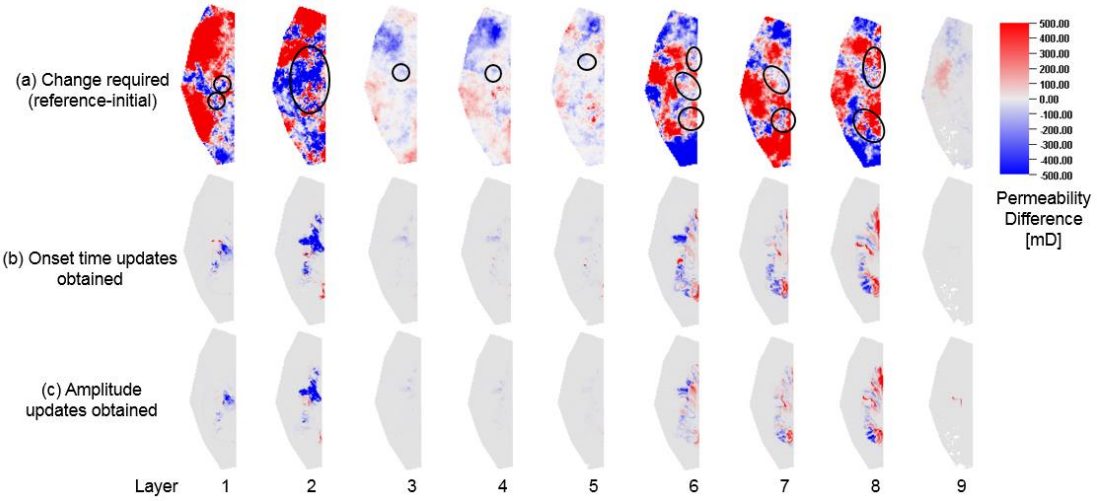

Figure 4.19 Comparison of permeability change for all layers with black circles indicating areas with similar permeability updates, (a) change required (reference - initial), (b) onset time updates obtained (onset time updated - initial), (c) amplitude updates obtained (amplitude updated - initial) (reprinted with permission from Liu et al., 2018)

Both updated models give better water cut matches than the initial model. Among 20 producers, all the wells with water broken through show improved water cut

predication than the initial model. Two wells, producer 3 and 16 are shown as representatives in Figure 4.20.

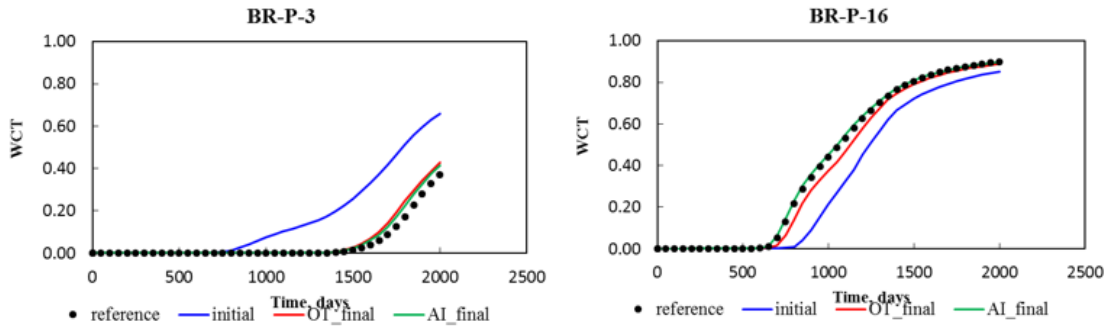

Figure 4.20 Comparison of water cut predication for producer 3 and producer 16

However, the onset time approach is more efficient and converges faster than the amplitude inversion method. The following Figure 4.21 shows the comparison of the reduction of normalized data misfit and the CPU time. Clearly, it shows that the onset time inversion method converges much faster than the amplitude inversion method, obtaining 2 times more error reduction after 15 iterations. Additionally, the onset time is around 6 times faster than the amplitude inversion method, resulting from the significant data reduction by integrating a single onset time map rather than 5 acoustic impedance change maps.

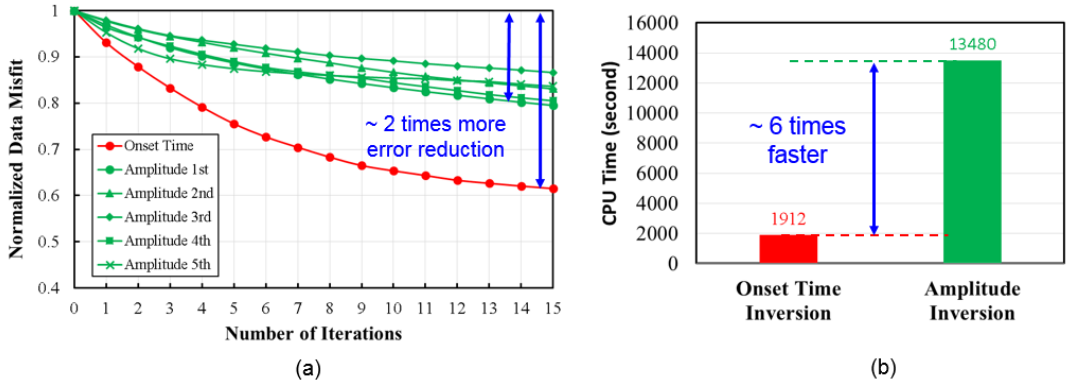

Figure 4.21 Comparison of the inversion performance, (a) reduction of normalized data misfit, (b) CPU time

The superior convergence performance of onset time method results from its advantage of being more linear than the amplitude inversion method. The spatial nonlinearity of the last iteration of these two methods are compared in the following Figure 4.22. The maximum nonlinearity value for each iteration are compared in Figure 4.23. Clearly, it can be seen that the nonlinearity of onset time method is not only much sparser in space but also much smaller in magnitude. Figure 4.23 shows that the onset time is more linear than the amplitude inversion method by 6~7 orders of magnitude.

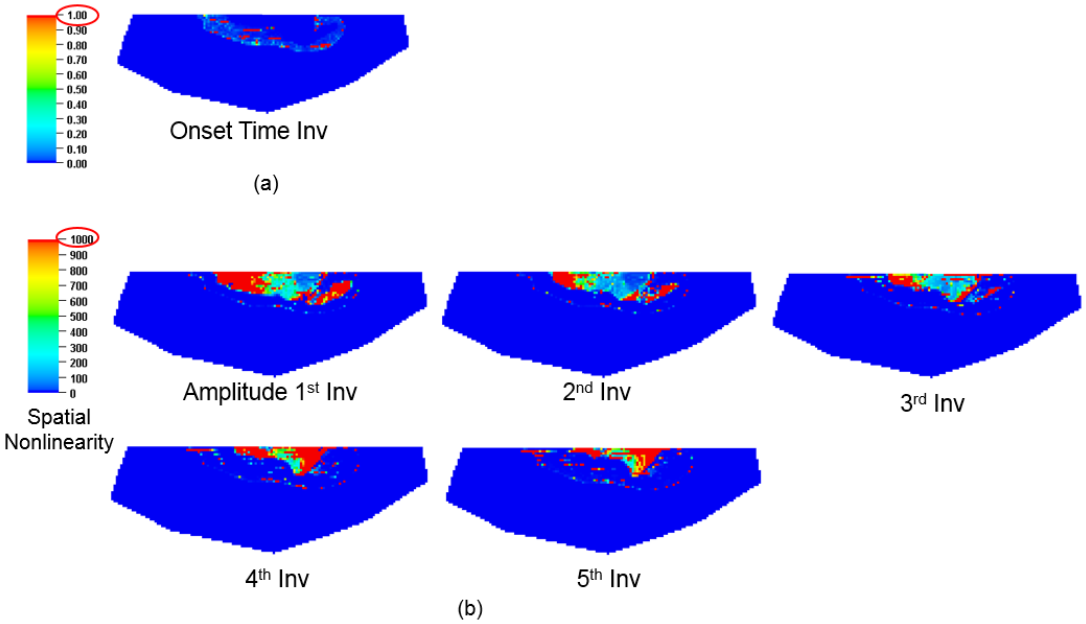

Figure 4.22 Comparison of the spatial nonlinearity of the last iteration (layer 7), (a) onset time inversion, (b) amplitude inversion of the first to fifth AI change maps

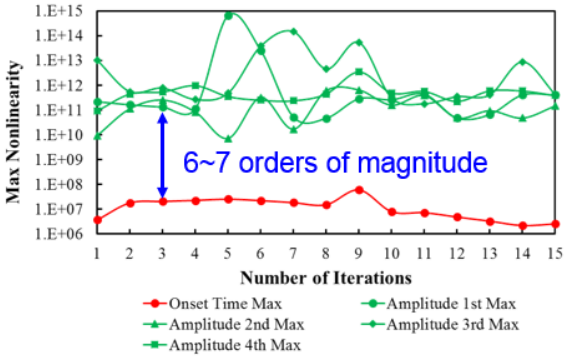

Figure 4.23 Comparison of maximum nonlinearity of each iteration

The smaller nonlinearity of the onset time inversion method can be attributed to the attractive quasi-linear properties of travel-time matching method, which are well documented in the geophysical literatures (Luo and Schuster et al., 1991a and 1991b; Zhou et al., 1995). The merit of working with skeletalized data (travel-time or seismic onset

time) lies in the fact that the skeleton data may be strongly influenced by only one type of model parameter and can lead to quasi-linear misfit function. However, working with raw data (seismic amplitudes) may result in a highly non-linear misfit function, which can easily get stuck in local minima, leading to inadequate history match (Luo and Schuster et al., 1991a and 1991b; Cheng et al., 2005).

The comparison of the onset time sensitivity and amplitude sensitivity of the last iteration is shown in Figure 4.24. The onset time sensitivity is more focused on the saturation fronts, which clearly indicates the propagation of fluid saturation fronts. However, the amplitude sensitivity is more diffused over the entire region.

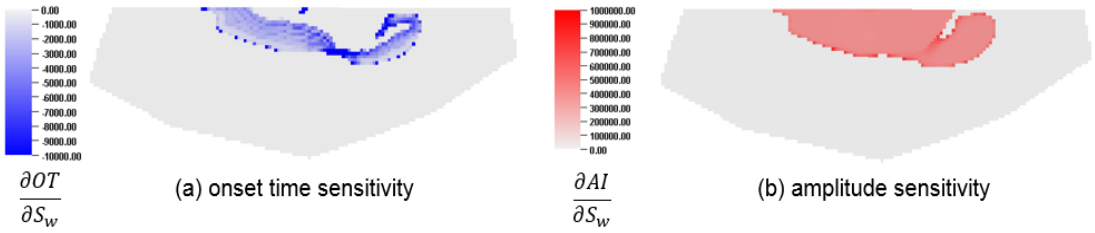

Figure 4.24 Comparison of the sensitivity of last iteration, (a) onset time sensitivity, (b) amplitude sensitivity

4.5 Summary

In this chapter, the onset time approach is compared with the traditional amplitude inversion method for integrating time-lapse seismic data. The effectiveness of the onset time method is demonstrated with both 2D synthetic case and Brugge benchmark case. It is shown that onset time obtains comparable model update while being more efficient, resulting from the significant data reduction achieved by integrating a single onset time map than multiple sets of amplitude maps.

In addition, the onset time inversion method has faster convergence rate than the amplitude inversion method. The nonlinearity associated with these two methods are quantitatively investigated. It is shown that the onset time has sparser nonlinearity than the amplitude method, resulting from the sparser onset time sensitivity. Moreover, the onset time nonlinearity is shown to be smaller than the amplitude nonlinearity by several orders of magnitude, resulting in the superior convergence performance.

CHAPTER V

CONCLUSIONS AND RECOMMENDATIONS

In this Chapter, the conclusions drawn from this study and recommendations for future work are discussed.

5.1 Conclusions

Onset time approach has shown great advantages for integrating frequent seismic data owing to the significant data reduction achieved by compressing multiple sets of seismic amplitude maps into a single onset time map. Also, it is shown to be less sensitive to the choice of petro-elastic model, making it a more robust method against the uncertainty in the seismic interpretation. In this study, I have investigated the feasibility of onset time approach for integrating infrequent seismic data. Sensitivity analysis are conducted based on the frequent seismic data of Peace River field. Additionally, I compared the inversion performance of onset time inversion method with the traditional seismic amplitude inversion method using both 2D synthetic and Brugge benchmark model. The main conclusions are summarized as follows.

(1) The onset time approach has been extended for integrating infrequent seismic data with the use of interpolation. The sensitivity analysis of the impact of seismic survey frequency shows that a clear onset time map can still be extracted from the infrequent seismic data, while interpolation is required for obtaining accurate and meaningful onset time values.

(2) Different interpolation methods were compared for calculating the onset time map for infrequent seismic data. It turns out that linear interpolation is more robust and more efficient, while the Lagrange interpolation is more difficult to implement and suffers from the risk of overfitting and requires more computational cost.

(3) The onset time will break if there is a change in the dominant physics that is not captured by the insufficient seismic surveys, such as changing from saturation dominated case to pressure and temperature dominated case. Because the change in the dominant physics will result in the change of seismic response, in that case, the linear interpolation may not give an accurate approximation to the true seismic response.

(4) The sensitivity analysis on the selection of threshold value shows that the threshold value should be set above the noise level to overcome the noise effects. Also, it should be smaller than the maximum change in the seismic signals to obtain a clear and adequate onset time map.

(5) The inversion performance of the onset time inversion method with traditional seismic amplitude inversion method was compared. Both the 2D synthetic case and Brugge benchmark case show that onset time inversion method obtains comparable model update while being much more efficient because of the significant data reduction obtained by converting multiple sets of seismic data into a single onset time map.

(6) The Brugge case shows that the onset time approach is not only more efficient, but also is a great tool for efficient imaging of the change in the reservoir, facilitating the dynamic reservoir management.

(7) The nonlinearity associated with the onset time inversion and amplitude inversion method was quantitatively investigated. It is found that the onset time nonlinearity is not only much sparser, but also is smaller than the amplitude nonlinearity by several orders of magnitude. The smaller onset time nonlinearity results from the use of skeletalized data (such as the travel-time or seismic onset time), which may be strongly influenced by only one type of model parameter (for example, the fluids saturation) and may lead to a quasi-linear misfit function. However, the raw data (such as the seismic amplitudes) could be significantly affected by multiple types of model parameters, which results in highly non-linear misfit function. The smaller onset time nonlinearity contributes to the superior convergence performance and more robust inversion result of the onset time inversion method.

5.2 Discussions on the Value of The Onset Time Approach

The onset time approach was initially proposed to for frequent seismic data integration, overcoming the difficulty of large amount of data by compressing multiple sets of seismic data into a single onset time map. It also shows the advantages in reducing the uncertainty in the seismic inversion results by being less sensitive to the petro-elastic model used to interpret the seismic data.

In this study, we have extended the onset time approach for infrequent seismic data with the use of interpolation. Although for infrequent seismic data, the advantages of data reduction are not as significant as that for frequent seismic data, the onset time approach still earns a lot of credits for being more robust and more linear than the traditional seismic amplitude inversion method.

However, the application of the onset time approach for infrequent seismic data in real situations should be considered. The major limitation of the onset time approach is that it requires multiple sets of time-lapse seismic data to resolve the onset time map. While for real cases, because of the large time interval between seismic surveys, the traditional seismic amplitude inversion method is actually a more natural way for seismic data integration once the fresh seismic survey data becomes available. In other words, the operator may not be willing to wait for several years until several seismic surveys are available and then try the onset time approach. However, in that sense, the onset time approach does provide an efficient way for reviewing and checking the amplitude inversion results. Because the onset time approach is less sensitive to the petro-elastic model, by comparing the results of onset time inversion with that of amplitude inversion, one can have some judgement on the reliability of the amplitude updated model.

On the other hand, because of the advantage of onset time approach for efficient reservoir imaging, the onset time approach can also be used for optimizing the seismic survey strategy. Because of the large cost associated with conducting seismic surveys, a common practice before deploying the seismic sensors is to use the prior reservoir model to predict the seismic response in the future to identify a proper time for conducting

seismic surveys and to determine the time interval between surveys. Owing to the advantages of onset time approach for visualizing the change in the reservoir, the optimization process can be done much more easily.

5.3 Recommendations for Future Work

The use of seismic data for quantitative calibration of reservoir models is an extremely challenging task. Although here we have extended the use of onset time approach for infrequent seismic data integration, extending its applicability, there is still much room existing for future improvement. Some ideas and recommendations for future work on onset time approach are discussed in the following.

(1) Hetz (2017) has shown that the onset time is sensitive to both permeability and porosity of the reservoir. In the study so far, we only focus on updating the permeability. It is recommended to implement the streamline-based inversion method for updating both the permeability and porosity simultaneously.

(2) One of the advantages of onset time approach for frequent seismic data (Hetz 2017) is that it is less sensitive to the noise in the data. However, in the infrequent seismic data, with interpolation, the noise will lead to some deviation in the calculated onset time value to the actual onset time. A suggestion to decrease the noise effect is to use interpolation first to calculate the interpolated onset time. Then, manually define several time intervals with relatively small time span. Then, take the time interval that the interpolated onset time falls in as the onset time. This method combines both the advantages of using interpolation and non-

interpolation, obtaining an accurate onset time while alleviating the effects of noise.

(3) In the study, it is found that the seismic response is more sensitive to the change of fluids saturation than the change of pore pressure. However, because the pressure front travels much faster than the fluid saturation front, the onset time of pressure, i.e. the arrival time of pressure front is hard to characterize. If we can find a good way to calculate the onset time for pressure front propagation, the effectiveness and applicability of the onset time approach could be further extended. For future work on this topic, it is recommended to start with the seismic data of the second phase (soaking and production period) of Peace River case, when the dominant physics is the depletion of pressure during production.

(4) So far, the primary benefits of the onset time approach for integrating infrequent seismic data is the large computational cost saved by data reduction. However, it would be very useful if the onset time approach can provide some guidelines for choosing the seismic survey frequency. This could save significant amount of cost associated with conducting seismic surveys.

(5) Onset time approach is found to be difficult in handling the time-lapse seismic data in the Norne field case (see Appendix D). It is suggested to try different ways to define the onset time to extract a clear and meaningful onset time map from the data.

REFERENCES

Bates, D.M. and Watts, D.G. 1980. Relative Curvature Measures of Nonlinearity. Journal of the Royal Statistical Society. Series B (Methodological): 1-25.

Behrens, R., Condon, P., Haworth, W. 2002. 4D Seismic Monitoring of Water Influx at Bay Marchand: The Practical Use of 4d in an Imperfect World. SPE Reservoir Evaluation & Engineering 5 (5): 410-420. DOI: 10.2118/79961-PA.

Cheng, H., Datta-Gupta, A., and He, Z. 2005. A Comparison of Travel-Time and Amplitude Matching for Field-Scale Production-Data Integration: Sensitivity, Nonlinearity, and Practical Implications. SPE Journal 10 (1): 75-90. DOI: 10.2118/84570-PA.

Datta-Gupta, A. and King, M. J. 2007. Streamline Simulation: Theory and Practice: Society of Petroleum Engineers. Original edition.

Dadashpour, M., Ciaurri, D.E., Mukerji, T. 2010. A Derivative-Free Approach for the Estimation of Porosity and Permeability Using Time-Lapse Seismic and Production Data. Journal of Geophysics and Engineering 7 (4): 351-368. DOI: 10.1088/1742-2132/7/4/002.

Dadashpour, M., Echeverría-Ciaurri, D., Kleppe, J. 2009. Porosity and Permeability Estimation by Integration of Production and Time-Lapse near and Far Offset Seismic Data. Journal of Geophysics and Engineering 6 (4): 325.

Duijndam, A. 1988a. Bayesian Estimation in Seismic Inversion. Part I: Principles1. Geophysical Prospecting 36 (8): 878-898.

Duijndam, A. 1988b. Bayesian Estimation in Seismic Inversion. Part II: Uncertainty Analysis1. Geophysical Prospecting 36 (8): 899-918.

Gassmann, F. 1951. Elastic Waves through a Packing of Spheres. Geophysics 16 (4): 673-685. DOI: 10.1190/1.1437718.

Grimstad, A.-A. and Mannseth, T. 2000. Nonlinearity, Scale, and Sensitivity for Parameter Estimation Problems. SIAM Journal on Scientific Computing 21 (6): 2096-2113.

He, Z., Yoon, S., and Datta-Gupta, A. 2002. Streamline-Based Production Data Integration with Gravity and Changing Field Conditions. SPE Journal 7 (4): 423-436.

Hetz, G., Kim, H., Datta-Gupta, A., King, M. J., Przybysz-Jarnut, J. K., Lopez, J. L., & Vasco, D. (2017, October 9). History Matching of Frequent Seismic Surveys Using

Seismic Onset Times at the Peace River Field, Canada. Society of Petroleum Engineers. DOI: 10.2118/187310-MS.

Hetz, G. (2017). Integration of Time Lapse Seismic Data Using Onset Time and Analysis of Spatial Resolution. Doctoral dissertation, Texas A & M University. Available electronically from http://hdl.handle.net /1969.1/169561.

Kennett, B. 1983. Seismic Wave Propagation in Stratified Media: Cambridge University Press Original edition. ISBN 0521239338.

La Follett, J. R., Wills, P., Lopez, J. L., Przybysz-Jarnut, J. K., & van Lokven, M. 2015. Continuous Seismic Reservoir Monitoring at Peace River: Initial Results and Interpretation. Society of Exploration Geophysicists. DOI: 10.1190/segam2015-5883275.1.

Landrø, M., Digranes, P., and Strønen, L. 2001. Mapping Reservoir Pressure and Saturation Changes Using Seismic Methods-Possibilities and Limitations. First break 19 (12): 671-684.

Landrø, M., Solheim, O.A., Hilde, E. 1999. The Gullfaks 4D Seismic Study. Petroleum Geoscience 5 (3): 213-226.

Liu, T. 2018. Seismic Onset Time Inversion Method for Infrequent Seismic Surveys. Society of Petroleum Engineers. DOI: 10.2118/194044-STU.

Lopez, J., Wills, P., La Follett, J. et al. 2015. Real-Time Seismic Surveillance of Thermal EOR at Peace River. In SPE Canada Heavy Oil Technical Conference: Society of Petroleum Engineers. ISBN 1613994028.

Luo, Y., and G. Schuster, 1991a, Wave equation traveltime inversion: Geophysics, 56, 645–653, doi:10.1190/1.1443081.

Luo, Y., and G. Schuster, 1991b, Wave equation inversion of skeletonized geophysical data: Geophysical
Journal International, 105, 289–294, doi:10.1111/j.1365-246X.1991.tb06713.x.

Mavko, G., Mukerji, T., and Dvorkin, J. 2009. The Rock Physics Handbook: Tools for Seismic Analysis of Porous Media: Cambridge university press. Original edition. ISBN 0521861365.

Mindlin, R. 1949. Compliance of Elastic Bodies in Contact. J. of Appl. Mech. 16.

Mindlin, R.D. 1949. Compliance of Elastic Bodies in Contact. Journal of Applied Mechanics 16: 259-268.

Paige, C.C. and Saunders, M.A. 1982. LSQR: An Algorithm for Sparse Linear Equations and Sparse Least Squares. ACM transactions on Mathematical Software 8 (1): 43-71.

Peters, L., Arts, R., Brouwer, G., Geel, C., Cullick, S., Lorentzen, R., Chen, Y., Dunlop, N., Vossepoel, F. and Xu, R. 2010. Results of the Brugge benchmark study for flooding optimization and history matching. SPE Reservoir Evaluation & Engineering 13 (3): 391-405. SPE 119094-PA. DOI: 10.2118/119094-PA.

Przybysz-Jarnut, J. K., Didraga, C., Potters, J. H. H. M., Lopez, J. L., La Follett, J. R., Wills, P. B., … Brouwer, D. R. 2015. Value of Information of Frequent Time-Lapse Seismic for Thermal EOR Monitoring at Peace River. Society of Petroleum Engineers. DOI:10.2118/175046-MS.

Rey, A., Bhark, E., Gao, K. 2012. Streamline-Based Integration of Time-Lapse Seismic and Production Data into Petroleum Reservoir Models. Geophysics 77 (6): M73-M87. DOI: 10.1190/Geo2011-0346.1.

Tang, J., Ehlig-Economides, C., Li, J., Guo, X., Wu, K., Mu, L., Tang, M., Du, X. 2018. Investigation of Multiple Hydraulic Fracture Propagation for Low-pressure Tight Sandstone Reservoirs in Northern Ordos Basin of Changqing Oilfield, China. In: The SPE International Hydraulic Fracturing Technology Conference and Exhibition, Muscat, Oman. SPE-191454-MS. doi: 10.2118/191454-18IHFT-MS.

Vasco, D.W., Yoon, S., and Datta-Gupta, A. 1999. Integrating Dynamic Data into High-Resolution Reservoir Models Using Streamline-Based Analytic Sensitivity Coefficients. Spe Journal 4 (4): 389-399. DOI: 10.2118/59253-Pa.

Vasco, D.W., Daley, T.M., and Bakulin, A. 2014. Utilizing the Onset of Time-Lapse Changes: A Robust Basis for Reservoir Monitoring and Characterization. Geophysical Journal International 197 (1): 542-556. DOI: 10.1093/gji/ggt526.

Vasco, D.W., Bakulin, A., Baek, H. 2015. Reservoir Characterization Based Upon the Onset of Time-Lapse Amplitude Changes. Geophysics 80 (1): M1-M14. DOI: 10.1190/Geo2014-0076.1.

Vasco, D.W. and Datta-Gupta, A. 2016. Subsurface Fluid Flow and Imaging: With Applications for Hydrology, Reservoir Engineering, and Geophysics: Cambridge University Press. Original edition. ISBN 1316577945.

Watanabe, S., Han, J., Hetz, G. 2017. Streamline-Based Time-Lapse Seismic Data Integration Incorporating Pressure and Saturation Effects. SPEJ Society of Petroleum Engineers.

Zhou, S., Huang, H. & Liu, Y. Pet. Sci. (2008) 5: 87. https://doi.org/10.1007/s12182-008-0015-3

Zhou, C., W. Cai, Y. Luo, G. Schuster, and S. Hassanzadeh, 1995, Acoustic wave-equation traveltime and waveform inversion of crosshole seismic data: Geophysics, 60, 765–773, doi:10.1190/1.1443815.

APPENDIX A

TIME OF FLIGHT SENSITIVITY CALCULATION

The time of flight (TOF) is defined as the travel time of a neutral tracer along a streamline trajectory (Datta-Gupta,& King, 2007), which is given by

$$\tau(\psi) = \int_{\psi} s(x)dr \,, \tag{1}$$

where ψ is the streamline trajectory, r is distance along the streamline. s is the slowness defined by the reciprocal of the interstitial velocity, which is shown in the Eq.2.

$$s(\boldsymbol{x}) = \frac{1}{|\vec{v}(\boldsymbol{x})|} = \frac{\phi(\boldsymbol{x})}{\lambda_{rt} k(\boldsymbol{x}) |\nabla P|} \tag{2}$$

Based on Darcy's law, λ_{rt} is the total relative mobility, $\lambda_{rt} = \lambda_{ro} + \lambda_{rw} + \lambda_{rg}$, and $|\nabla P|$ is the pressure gradient along the streamline. Because the slowness is a composite quantity involving reservoir properties, its first order variation, assuming a fixed pressure gradient, will be given by

$$\delta s(\boldsymbol{x}) = \frac{\partial s(\boldsymbol{x})}{\partial k(\boldsymbol{x})} \delta k(\boldsymbol{x}) + \frac{\partial s(\boldsymbol{x})}{\partial \phi(\boldsymbol{x})} \delta \phi(\boldsymbol{x}) . \tag{3}$$

From Eq.2, the partial derivatives are then simply computed as the following.

$$\frac{\partial s(\boldsymbol{x})}{\partial k(\boldsymbol{x})} \approx \frac{-\phi(\boldsymbol{x})}{\lambda_{rt} \left(k(\boldsymbol{x})\right)^2 |\nabla P|} = -\frac{s(\boldsymbol{x})}{k(\boldsymbol{x})} \tag{4}$$

$$\frac{\partial s(\boldsymbol{x})}{\partial \phi(\boldsymbol{x})} \approx \frac{1}{\lambda_{rt} k(\boldsymbol{x}) |\nabla P|} = \frac{s(\boldsymbol{x})}{\phi(\boldsymbol{x})} \tag{5}$$

In Eq.4 and Eq.5**,** it is assumed that local perturbations in permeability or porosity generated by pressure changes can be neglected. This assumption means that streamlines do not shift because of these small perturbations. By integrating along each streamline trajectory, the relationship between the change in the TOF ($\delta\tau$) and the change in slowness can be written as

$$\delta\tau(\psi) = \int_{\psi} \delta s(x) dr = \int_{\psi} \left[\frac{\partial s(x)}{\partial k(x)} \delta k(x) + \frac{\partial s(x)}{\partial \phi(x)} \delta\phi(x) \right] dr \,. \tag{6}$$

The tracer travel time sensitivity along a single streamline, ψ, with respect to permeability and porosity at location x, follows Eq.6 by integrating from the inlet to the outlet of the streamline within the grid block,

$$\frac{\delta\tau(\psi)}{\delta k(\boldsymbol{x})} = \int_{\text{inlet}}^{\text{outlet}} \left[-\frac{s(\boldsymbol{x})}{k(\boldsymbol{x})} \right] dr = -\frac{\Delta\tau(\boldsymbol{x})}{k(\boldsymbol{x})}, \tag{7}$$

$$\frac{\delta\tau(\psi)}{\delta\phi(\boldsymbol{x})} = \int_{\text{inlet}}^{\text{outlet}} \left[\frac{s(\boldsymbol{x})}{\phi(\boldsymbol{x})} \right] dr = \frac{\Delta\tau(\boldsymbol{x})}{\phi(\boldsymbol{x})}. \tag{8}$$

Here $\Delta\tau(x)$ is the time-of-flight across the grid block at location x.

APPENDIX B

SATURATION FRONT ARRIVAL TIME SENSITIVITY

We now relate the time of flight sensitivity to the travel time sensitivity of the water saturation. Consider two-phase incompressible flow of oil and water described by the Buckley-Leverett equation written using the streamline time-of-flight as the spatial coordinate (Datta-Gupta,& King, 2007) ,

$$\frac{\partial S_w}{\partial t}+\frac{\partial F_w}{\partial \tau}=0. \tag{9}$$

The velocity of a given saturation, S_w, along a streamline, ψ, is given by the slope of the fractional flow curve,

$$\left(\frac{\partial \tau}{\partial t}\right)_{S_w}=\frac{dF_w}{dS_w}. \tag{10}$$

This equation relates the travel time of a saturation, $t\left(S_w,\ \tau;\psi\right)$ to the TOF τ .We can now compute the sensitivity of the saturation arrival time using that of the streamline TOF as follows

$$\frac{\delta t\left(S_w,\ \tau;\psi\right)}{\delta k\left(\boldsymbol{x}\right)}=\frac{\delta \tau\left(\psi\right)}{\delta k\left(\boldsymbol{x}\right)}\Big/\frac{dF_w}{dS_w}, \tag{11}$$

$$\frac{\delta t\left(S_w,\ \tau;\psi\right)}{\delta \phi\left(\boldsymbol{x}\right)}=\frac{\delta \tau\left(\psi\right)}{\delta \phi\left(\boldsymbol{x}\right)}\Big/\frac{dF_w}{dS_w}. \tag{12}$$

After water breakthrough on a streamline, these arrival times are evaluated at the total time of flight, $\tau\left(\psi\right)$, for the streamline.

APPENDIX C

WATER SATURATION SENSITIVITY CALCULATION

Our goal here is to derive expressions for the sensitivity of water saturation with respect to variations in permeability. In two phase flow, water saturation is a function of the streamline TOF, τ and time, t . We consider a self-similar solution to Eq.9, where the saturation is a function of the dimensionless ratio τ / t . This allows us to relate the derivative of saturation with respect to time, to the derivative with respect to τ , which can be written as the following.

$$\frac{\partial S_w}{\partial t} = -\frac{\tau}{t^2}\frac{dS_w(\tau/t)}{d(\tau/t)} \tag{13}$$

$$\frac{\partial S_w}{\partial \tau} = \frac{1}{t}\frac{dS_w(\tau/t)}{d(\tau/t)} \tag{14}$$

Hence,

$$\frac{\partial S_w}{\partial \tau} = -\frac{t}{\tau}\frac{\partial S_w}{\partial t}, \tag{15}$$

leading us to the water saturation sensitivity:

$$\frac{\delta S_w(\tau,t)}{\delta k(x)} = \frac{\partial S_w}{\partial \tau}\frac{\delta \tau}{\delta k(x)} = -\frac{t}{\tau}\frac{\partial S_w}{\partial t}\frac{\delta \tau}{\delta k(x)}. \tag{16}$$

We calculated the partial derivative of water saturation with respect to time in Eq.16 by using a backward time difference as

$$\frac{\partial S_w(\tau,t)}{\partial t} \approx \frac{S_w(\tau,t) - S_w(\tau,t-\Delta t)}{\Delta t}. \quad (17)$$

Here Δt is the timestep size. This requires saving the saturation information for the time step immediately prior to the time lapse survey time. Therefore, the saturation sensitivity at location, τ, at a given time, t, can be calculated by:

$$\frac{\delta S_w(\tau,t)}{\delta k(x)} = -\frac{t}{\tau}\frac{S_w(\tau,t) - S_w(\tau,t-\Delta t)}{\Delta t}\frac{\delta \tau}{\delta k(x)}, \quad (18)$$

where the last partial derivative of travel time, with respect to permeability, can be obtained from Eq.7. In this paper, we calibrate against the changes in saturation, rather than the saturation itself. The generalization of the sensitivity calculation to account for these effects can be found in Watanabe et al. (2017).

APPENDIX D

ONSET TIME FOR NORNE FIELD CASE

As shown in section 3.4, the onset time will break for infrequent seismic data if there is a change in the dominant physics that is not captured in the seismic surveys. In addition, the onset time approach also appears to have difficulty in handling the 4D seismic data in the Norne field case.

The Norne field is an offshore sandstone reservoir located in the northern part of Norway. The field was discovered in 1991 and started to produce in 1997. As shown in Figure A-1, the geologic model consists of more than 120,000 cells and contains two different rock types separated by a shale layer that hydraulically disconnects the stratigraphic layers above and below. The first rock type comprises the upper layers (layer 1 to 3), which is saturated by gas. The second rock type is located below the shale layer, which contains the oil zone and bottom aquifer. The reservoir model consists of 44,431 active cells and 36 wells (9 injectors and 27 producers). A detailed reservoir model was provided as an initial model for inversion. Between 2001 and 2006, 4 sets of time-lapse seismic data were acquired on a 1-year or 2-year frequency. The acquired seismic data were translated into acoustic impedance maps as shown in Figure A-2 (a). In addition to the seismic data, history production data were also available in the form of water, oil, gas rates, and bottom-hole pressure at producers.

In this study, we focus on exploring the feasibility of onset time approach for integrating the time-lapse seismic data in the Norne field. And the history production data is used to verify the inversion results.

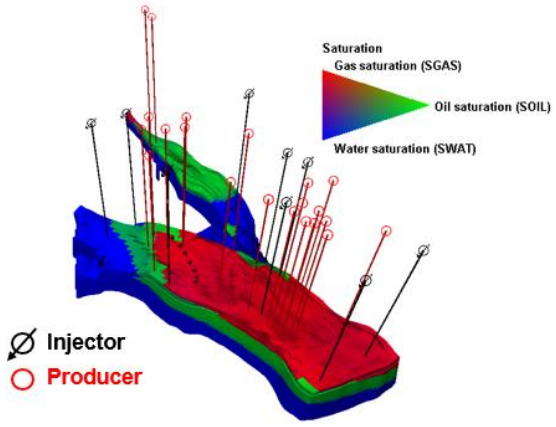

Figure A-1 Norne field structure, red shows the gas cap, green represents the oil zone and blue indicates the bottom aquifer

The dominant physics in the field is the upwards movement of the bottom aquifer, which results in the increasing acoustic impedance value of formation. Thus, the onset time should be defined in a way where the arrival of water front could be characterized. To obtain an indicative onset time map, various methods to define the onset time and different threshold values have been tested. After comparing the different calculated onset time maps, the best case observed is using a threshold value of an increase of 0.5% of initial or background value. The observed onset time map is shown in the following Figure A-2 (b).

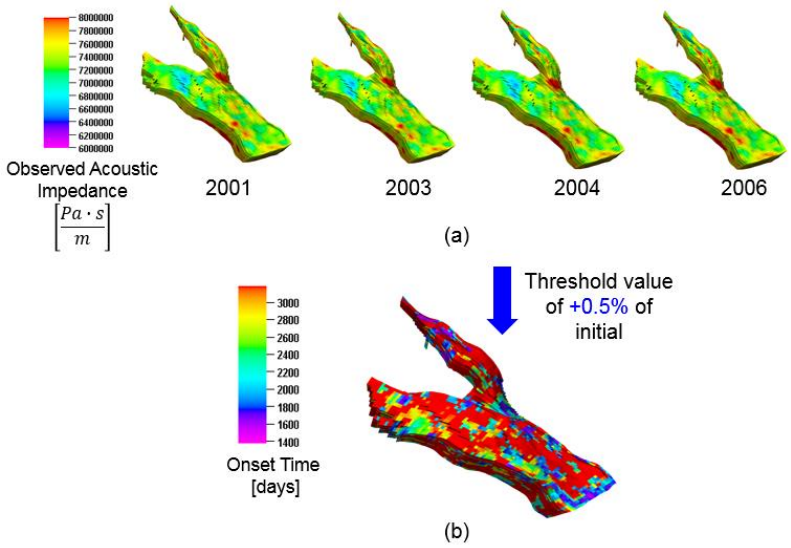

Figure A-2 (a) 4 sets of observed acoustic impedance maps, (b) observed onset time map

A comparison of the observed onset time map and the initial onset time map based on the initial model for selected layers is shown in Figure A-3 (a) and (b). It can be seen that in the initial map, clear onset time pattern (‘purple-blue’ spatial distribution) is observed. However, in the observed onset time map, the onset time pattern is much more scattered and diffused.

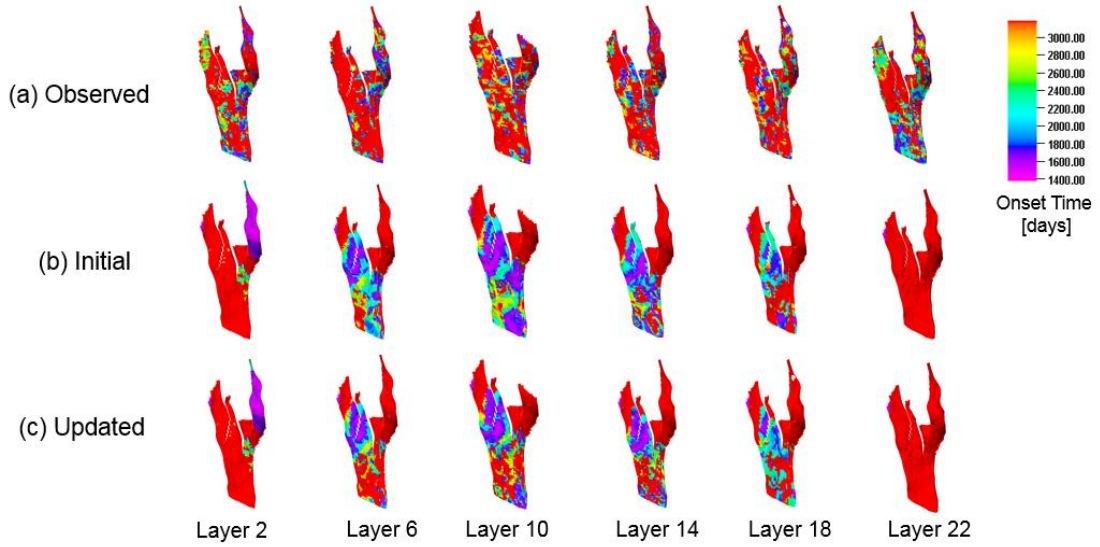

Figure A-3 Comparison of onset time maps for selected layers, (a) observed, (b) initial, (c) updated

Having tested different threshold values, the various observed onset time maps all failed to show a clear pattern, indicating that the potential reason could be large noise in the observed seismic data. This is typically true for offshore time-lapse seismic surveys because of the shifting sensor location and spacing. On the other hand, it is also possible that the petro-elastic model is not accurate enough for interpreting the observed seismic data. Thus, the observed acoustic impedance maps are quite different from the initial acoustic impedance maps, as shown in Figure A-4. The large difference between the observed and initial acoustic impedance maps might be also resulted from the large discrepancy between the initial model and the true model.

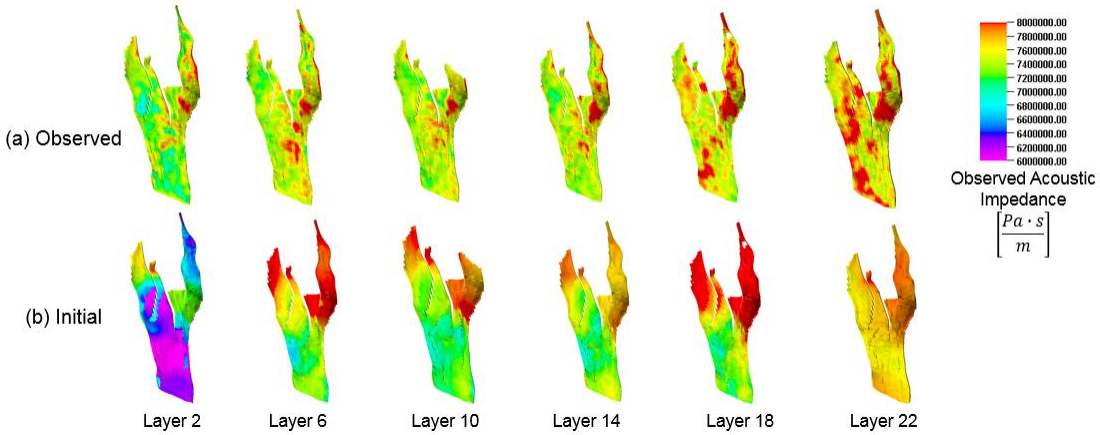

Figure A-4 Comparison of observed acoustic impedance map and initial acoustic impedance map for selected layers

The difference between the observed seismic data and initial simulated seismic response can also be observed by comparing the acoustic impedance change maps, as shown in Figure A-5. The red color in Figure A-5 represents the increase in the acoustic impedance value resulting from the increasing water saturation, while the blue color represents the decrease in the acoustic impedance value, which is affected by the increasing pressure because of water injection. In the simulated results, the pressure effect is not as obvious as in the observed map.

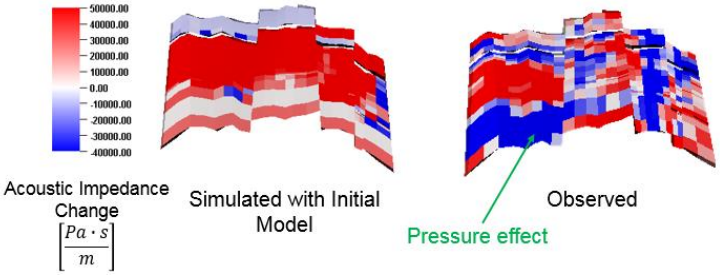

Figure A-5 Comparison of acoustic impedance change between simulated seismic response and observed seismic response

The red color showing in the simulated result shown in Figure A-5 results from the upwards movement of oil-water contact, which is clearly shown in the increasing water saturation between 2001 and 2006 in Figure A-6.

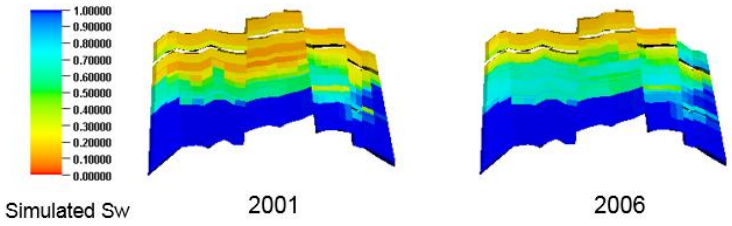

Figure A-6 Comparison of water saturation of 2001 and 2006 (cross-sectional view)

Although the observed onset time map does not seems to be clear and meaningful, efforts still have been made to try to run the onset time inversion based on the observed onset time map (Figure A-3 (a)). The reduction in the normalized data misfit is shown in the following Figure A-7 and the model update is shown in Figure A-8.

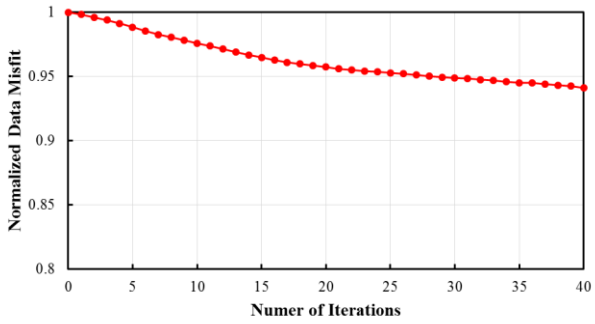

Figure A-7 Reduction in the normalized data misfit

It can be seen that the reduction in the normalized data misfit is extremely slow and the model update is quite extreme. The history production data is used to verify if the update in the permeability field is reliable. The results show that among 20 producers with

available history data, there are 4 wells showing improved water cut predication (Figure A-9). In addition, 4 wells does not show much improvement (Figure A-10). However, the rest 12 wells show much worse water cut predications (Figure A-11).

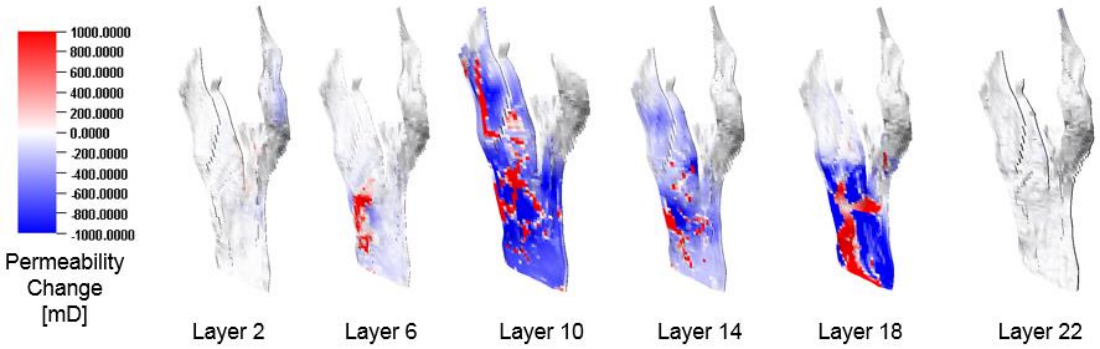

Figure A-8 Update in permeability

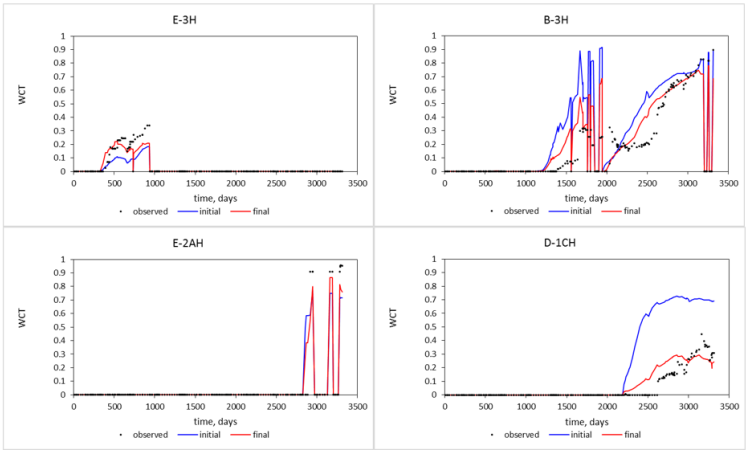

Figure A-9 Wells with improved water cut predication

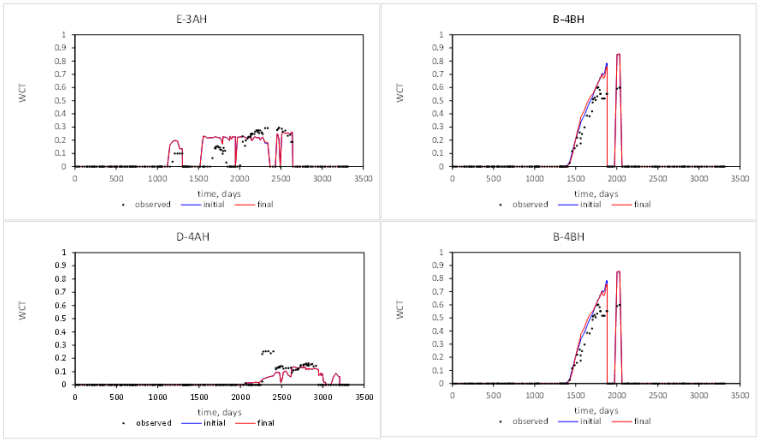

Figure A-10 Wells without much improvement

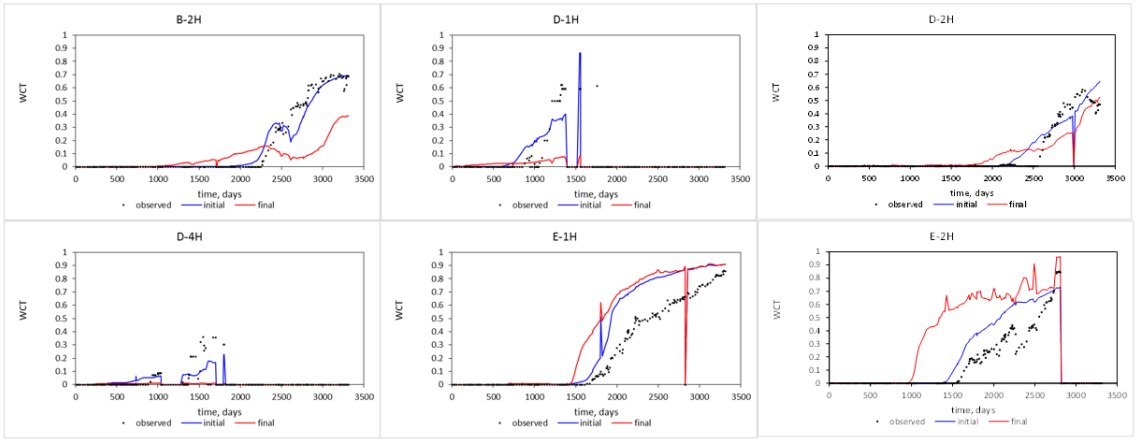

Figure A-11 Selected wells with worse water cut predication

The bad match in the history production data indicates that the model update with the observed onset time map is not reliable. The potential reasons are summarized in the following.

(1) The observed seismic data is too noisy because of the shifting sensor location and spacing when conducting offshore seismic surveys. Thus, no clear onset time pattern can be extracted.

(2) The initial model is too far away from the true model, leading to large difference between the observed onset time map and initial onset time map.

(3) The petro-elastic model used to interpret the seismic data and seismic inversion is not accurate.

For future study on the onset time approach with Norne field seismic data, it is recommended to try different ways to define a clear and indicative onset time, such as using the time at which the largest derivative or the peak change occurs, etc.